

Filtered Partial Differential Equations: a robust surrogate constraint in physics-informed deep learning framework

Dashan Zhang^a, Yuntian Chen ^{*b}, and Shiyi Chen ^{†b, a}

^aDepartment of Mechanics and Aerospace Engineering, Southern University of Science and Technology, Shenzhen 518055, China

^bNingbo Institute of Digital Twin, Eastern Institute of Technology, Ningbo, China

Abstract

Embedding physical knowledge into neural network (NN) training has been a hot topic. However, when facing the complex real-world, most of the existing methods still strongly rely on the quantity and quality of observation data. Furthermore, the neural networks often struggle to converge when the solution to the real equation is very complex. Inspired by large eddy simulation in computational fluid dynamics, we propose an improved method based on filtering. We analyzed the causes of the difficulties in physics informed machine learning, and proposed a surrogate constraint (filtered PDE, FPDE in short) of the original physical equations to reduce the influence of noisy and sparse observation data. In the noise and sparsity experiment, the proposed FPDE models (which are optimized by FPDE constraints) have better robustness than the conventional PDE models. Experiments demonstrate that the FPDE model can obtain the same quality solution with 100% higher noise and 12% quantity of observation data of the baseline. Besides, two groups of real measurement data are used to show the FPDE improvements in real cases. The final results show that FPDE still gives more physically reasonable solutions when facing the incomplete equation problem and the extremely sparse and high-noise conditions. For combining real-world experiment data into physics-informed training, the proposed FPDE constraint is useful and performs well in two real-world experiments: modeling the blood velocity in vessels and cell migration in scratches.

Keywords: Filtered equations, Physics informed, Low-quality observation, Data restoration.

1 Introduction

Deep learning is one of the most powerful methods for fitting an unknown data distribution. In this section, a brief introduction of the physics-informed framework is made as the background knowledge. This framework utilizes the governing equation to better solve problems and increase the model's performance. Meanwhile, we demonstrate the challenge inherent in this framework with some examples. Due to the complexity of the original equations, the optimization of the neural network becomes difficult. Therefore, the idea of using surrogate equations to simplify the problem is raised. Correspondingly, this improvement can alleviate the dependence on the quality and quantity of data in physics-informed training.

1.1 Background of solving PDE via NN

Since the dawn of science, humans have been finding and solving equations to describe the world. The differential equations are the equations containing derivatives of unknown variables, and solving the differential equations is one of the most fundamental problems in physics and mathematics. The ordinary differential equation (ODE) has a unique solution when the Lipschitz continuity condition is satisfied[1],

*Corresponding author: ychen@eias.ac.cn

†Corresponding author: chensy@sustech.edu.cn

but the partial differential equation (PDE) doesn't have such good properties. Therefore, many numerical methods have been designed and used to find the approximate solutions of PDEs by simulation.

With the development of artificial intelligence, data-driven models are widely used in many disciplines [2, 3, 4, 5]. The Neural network (NN) models show their strong fitting ability in Computer version[6] (CV) and Natural language processing[7] (NLP) field. In the field of engineering computation, the Fourier neural operator (FNO) is proposed to learn the features in Spectral space[8]; deconvolutional artificial neural network (DANN) is developed for subgrid-scale (SGS) stress in large eddy simulation (LES) of turbulence[9]; generative adversarial network (GAN) is also used to generate complex turbulence under the condition of missing data due to its good fidelity[10]. Strong abstract ability enables NN to learn the embedding mapping in most of training datasets. With the gradient decent[11] method, the NN can learn the pattern, which is the relationship of different features from the data in the optimization process. Many kinds of NN architecture are raised, such as the convolutional block[12] and the self-attention block[13], to treat different features. But when the data is insufficient to cover the features in embedding space, can we add some domain knowledge to help optimization?

The paradigms that add equation constraints into the optimization process of NN, such as the physics-informed neural network[14] (PINN), provide a beautiful vision of solving PDE with domain knowledge automatically. Training with explicit physical constraints (e.g., the governing equations) can lead to better results. In the past four years, physics-informed based methods have been proposed and applied in various fields. In the physics-informed based problem, some scientific machine learning frameworks are proposed (e.g., the DeepXDE[15], AutoKE[16] and NeuroDiffEq[17] framework) to solve the differential equations. In the inverse problem of physics-informed learning, the model is built for the equation discovering. Scholars have proposed many methods that can work in the knowledge discovery field[18], the sparse regression method is capable of discovering the PDEs in given system[19]; the deep learning has also been proved to be effective on the physics-informed inverse problem (e.g., the DL-PDE[20]); the symbolic genetic algorithm (SGA-PDE) can be used to discover the open-form PDEs[21].

In the view of application, physics-informed framework has improved the model performance in many scenarios: using the physical laws in power systems, NN can model the power system behavior both in steady-state and in dynamics[22]; the theory-guided deep-learning load forecasting (TgDLF) model the future load through load ratio decomposition with the considered historical load, weather forecast and calendar effect.[23]; with acoustic wave equation, NN can identify and characterize a surface breaking crack in a metal plate[24]; with the advection-diffusion equations, NN can obtain better super-resolution outputs in the images of atmospheric pollution[25]; in the field of geophysics, NN can better model the subsurface flow with the guiding of theory (e.g., governing equations, engineering controls and expert knowledge)[26].

Different from the numerical simulation method, the universal approximation theorem shows that a NN is able to approximate any continuous function on a compact subset of \mathcal{R}_n with sufficient precision when it has enough parameters[27]. Therefore, it is theoretically possible to find the solution of any equation only with PDE constraints as long as the equations are closed. Considering that the optimization process of NN can be summarized as 'finding the parameters to minimize the given loss function', the equations can be added into the loss function to make NN solve PDE automatically. When facing a complex problem, adding some simulation or measurement data points to help NN determine the large-scale distribution of solutions is a common method. In the following, we refer to these data points as 'observation points'.

Regarding solving equations, the Navier-Stokes[28] (N-S) equation in fluid mechanics is one of the most challenging problems. The N-S equation (Eq.1), as one of the basic equations of the Millennium Prize Problems, based on the fluid micelle hypothesis, describes the motion of viscous fluid substances. And the continuity equation (Eq.2) describes the mass conservation of fluid particles (Eq.2 is the incompressible case). The solution[29] and improved simulation[30] of the N-S equation are important in both theory and engineering.

$$\frac{\partial u}{\partial t} + u \cdot \nabla u = -\frac{1}{\rho} \nabla p + \nu \nabla^2 u \quad (1)$$

$$\nabla \cdot u = 0 \quad (2)$$

where u, p, ρ, ν represent the velocity vector, pressure, density and dynamic viscosity, respectively.

In this paper, the cylinder flow is used as an example to demonstrate the difficulties found in physics-informed training. We propose our improved method and verify it in various cases. The cylinder flow, governed by the N-S equation, is a classic example which can reflect the properties of the fluid[31]. In the cylinder flow case, the boundary condition (BC) describes a cylinder wall in the flow field generally. In Eq.3, the velocity u is limited to zero on the surface of the cylinder wall, where r is the radius of the cylinder wall. The simulation solution reflects the flow in Fig.1.

$$u(r \cdot \cos\theta, r \cdot \sin\theta) = (0, 0), \theta \in [0, 2\pi] \quad (3)$$

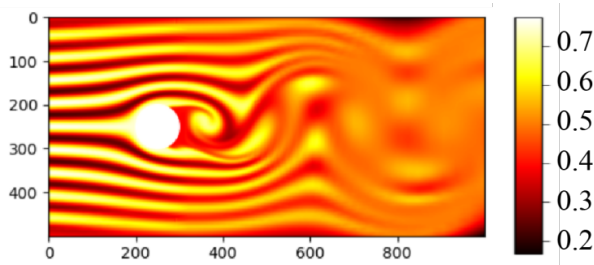


Fig. 1. The fluid flow through a cylinder wall (streak-lines). To keep the consistency of data, the reference simulation solutions are from the open-resource data of Hidden fluid mechanics, HFM[32]

In recent years, many scholars have used NN to solve the problems and inverse problems of the cylinder flow. Though it is an under-determined problem, the velocity field restoration from concentration field is solved well by NN[32]. In the knowledge discovery field, NN can abstract the N-S equation from the velocity field of cylinder flow with high precision[19]. To a certain extent, these works show that NN can describe the solution of the N-S equation. However, current works still strongly depend on the quality and quantity of observation data, thus training based on low quality (i.e., noisy and sparse) data is still an open question.

In general, using physical constraints to improve the NN modeling ability of observation data is a powerful method. But it has high requirements for the quality and quantity of data. When it comes to the modeling of real measurement data, it is important to better model the sparse and noisy data.

1.2 Current challenges

There is no such thing as a free lunch, and finding a good approximate solution only with PDE constraints is quite difficult. The optimization problem of NN is always a non-convex due to the non-linear part inside (optimization of a single hidden-layer NN with non-linear activation function has been proved to be a non-convex problem)[33]. Finding the optimal solution with a gradient-based method is NP-hard because the problem is non-convex. As a result, the majority of constructive works usually used more informative data in training (e.g., the observation data of concentration in the full domain on HFM[32]).

According to the relationship between the observation and the test domain, the physics informed problem can be divided into three different tasks (as shown in Fig.2). When the observation points all locate outside the desired interval (red test domain in Fig.2), the task of the NN is essentially extrapolation(Fig.2.a). When the observation points are sampled in the same interval of the test domain, the task is called restoration if the observation data is noisy or sparsely sampled from the observation points (Fig.2.b) or interpolation if the data is sufficient and accurate (Fig.2.c).

In this paper, we focus on the restoration task (i.e., Fig.2.b) since it is more common in practice. The NN is designed to learn the embedding distribution of solutions with noisy and sparse data. With the help of physical constraints, NN can provide more reasonable and accurate modeling results. The meaning of restoration is finding a better method to model the noisy and sparse data in the real experiment. The quantity and quality of data required for modeling can be greatly reduced, resulting in lower costs in practice.

As the complexity of the problem increases, more observation data is required to describe the distribution of the exact solution. In Fig.3, the first example of Burgers equation (Fig.3.a) shows NN giving

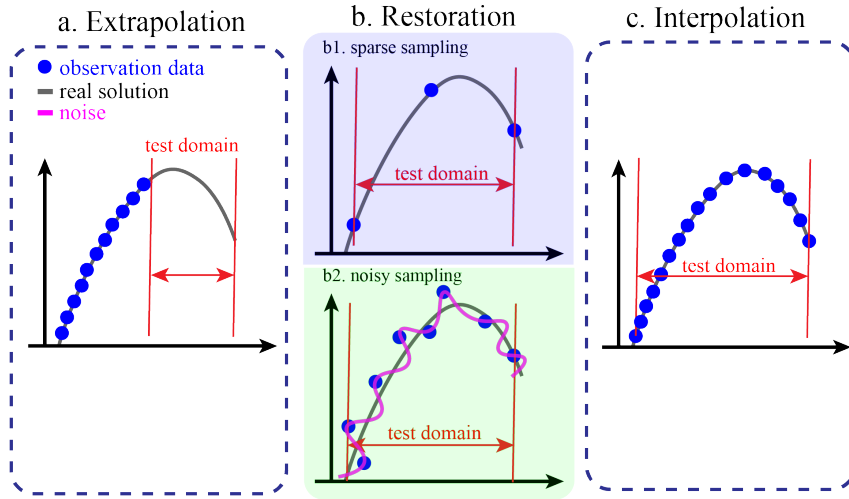


Fig. 2. Summary of the physics-informed training tasks. (a) The extrapolation, where known and unknown parts conform to the different data distributions. NN is trained to learn the hidden pattern in the known part, and extrapolate it in the unknown part. (b) The restoration, of which the given and unknown parts conform to the same data distribution. Meanwhile, the data has poor quality and quantity. b1 shows the restoration from sparse data, and b2 is the restoration from noisy data. (c) sufficient and accurate data with the same distribution, which makes the task an ordinary interpolation problem.

the incorrect solution in the interval with the larger differential term. Solutions of different viscosities show the effect of regularity in PDE solutions, which makes NN tend to give smoother outputs. The second example (Fig.3.b), a simple exponential function, directly shows that even though the equation is infinitely differentiable, NN fits worse when there is a magnitude gap between the scale of the differential terms. The last example is the cylinder flow (Fig.3.c) under the large Reynolds number (Re) condition, the complex velocity field makes NN converge to a trivial solution. Because of the frequent changes in velocity, NN fails to learn the embedding pattern and only provides the mean value to achieve the local optimum.

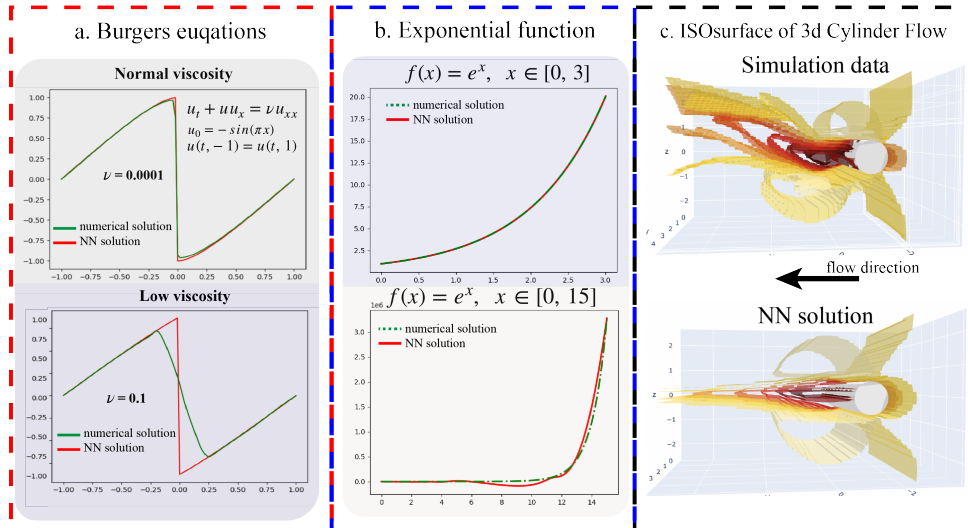


Fig. 3. The NN output guided by different equations. (a) The Burgers equation is the classic example in PINN[14], which is used to show the effect of regularity; (b) The exponential function, which shows the difficulty of NN to handle the interval with a small loss value. NN always focus on the large loss interval; (c) The N-S equation. Facing the complex solution, NN is tend to be trapped in the local minimum and obtain the trivial solution.

To summarize, the more complex the problem, the greater the amount of data required for training. The sparse and noisy data still contain little information about the solution's distribution, but most of

the missing information can be inferred using the PDE as domain knowledge. Although NN can infer most of the missing value, the observation data is still important because it acts as the fixed points in outputs, which anchor the large-scale solutions. The main area for improvement is how to use less or noisier observation data to train a better NN. More specifically, the current challenges of physics-informed training can be itemized as follows:

- The experiment always produces sparse quantities of data when the observation points are gathered through measurements. Lack of data causes NN solutions to frequently yield trivial solutions in complex problems (e.g., Fig.3.c).
- The measurement noise makes observation data out of line with the underlying governing equations. The noise in observation (especially at initial points) can seriously affect the NN optimization process.

In order to abstract more information from low-quality and low-quantity data, the equation constraints are improved. In this paper, we propose a new surrogate constraint for the conventional PDE loss using deep learning and numerical method filtering. The surrogate constraint takes the advantage of the meshless feature of NN, calculates the PDE loss with the filtered variables instead of the original PDE. The proposed method can be regarded as an intermediary layer based on filter operations, which maintains the equation’s form, and is unaffected by the NN architecture. In this paper, the proposed filtered PDE model (FPDE in short) shows the following contributions:

- The study proposes a filtered PDE framework that is inspired by large eddy simulation (LES). The solution of physics-informed training is more robust under the constraints of the proposed framework.
- In the noise experiments, the FPDE model can obtain the same quality solution with 100% higher noise than the baseline.
- In the sparsity experiments, the FPDE model can obtain the same quality solution with only 12% quantity of observation points of baseline.
- In the real-world experiments with missing equations, the FPDE model can obtain a more physically reasonable solution.

In a word, using FPDE as surrogate constraints makes NN better model the data distribution with noisy and sparse observations. This improvement is considerable, especially for the work relying on experimental data.

2 The motivation and ‘conflict’ theory

To better model the noisy and sparse data, one of the directions worth improving is the co-optimization between PDE and data loss. We discovered that the discrepancy between the directions of the PDE loss and the data loss contributes to some of the challenges in NN optimization. In this paper, the aforementioned challenge is defined as ‘conflict’ and its mathematical derivation is provided and discussed. In order to reduce the influence of conflict, an improved method is introduced. This improved method is inspired by the classic numerical method (i.e., large eddy simulation, LES)[34]. In this part, the incompressible N-S equation is used as an example for demonstration.

2.1 Mechanism of ‘conflict’

The deep neural network, usually optimized by the gradient-based method, provides a solving paradigm with a large number of parameters. With the classic loss function (i.e., mean squared error, MSE), the solving PDE by NN can be described as a soft-constraint method. Different from the hard-constraint numerical method, the soft-constraint method doesn’t constrain the calculation in each step, but only optimizes the final solution by loss function[23]. Under the soft constraint, the optimization process of the

parameters in NN is essential. The difficulties in the physics-informed framework can be demonstrated from the perspective of optimization.

In the physics-informed framework, the loss function can be written as Eq.4. The IC/BC loss is determined by the initial and boundary conditions; the PDE loss is calculated based on the collocation points, which are the given points only used to calculate PDEs and independent of the distribution of observation data. Given the PDE, initial, and boundary conditions, and the observation data jointly determining the final loss, NN training can be broadly defined as the co-optimization of these losses.

$$Loss = L_{data} + L_{PDE} + L_{ICBC} \quad (4)$$

where $L_{data} = \frac{1}{N} \|y - \hat{y}\|_2$ and $L_{PDE} = \frac{1}{M} \|residual\ PDE\|_2$. The L_{ICBC} is decided on the task specifically. y and \hat{y} represent the NN output and observation respectively.

The optimization direction of the model is the gradient direction of parameters update. It is jointly determined by the sum of each loss direction during each iteration of the multi-objective optimization in Eq.4. The direction of the loss functions in one optimization step can be written as the partial derivative terms in Eq.5, which shows the effect of the loss function on the parameters of NN.

$$\theta_t = \theta_{t-1} - \eta \left(\frac{\partial L_{data}}{\partial \theta_{t-1}} + \frac{\partial L_{pde}}{\partial \theta_{t-1}} + \frac{\partial L_{ICBC}}{\partial \theta_{t-1}} \right) \quad (5)$$

where θ_t represents the NN parameters in iteration t and η represents the learning rate (defined as hyper-parameter in advance).

Theoretically, there must exist a group of parameters that make PDE and data loss all close to 0. The closed PDEs have embedding distributions of the solutions, but the distribution may have complex pattern (i.e., the high frequency feature), which make NN hard to learn. Meanwhile, the observation data also maps the distribution of exact solutions. The physics-informed framework enables NN to learn both the intricate high-frequency patterns from the PDE constraint and the large-scale distribution from observation data. Therefore, having the same embedding distribution under different constraints is the premise of co-optimization.

In the ideal physics-informed framework, PDE and data constraints can help each other out of the local optimum. But in fact, the relationship between these two losses backfired in many practical problems. In the training of physics-informed task, the optimized function is always the residual form of the governing equations, which is the difference between the left and right hand sides of the equation. The 2-dimensional N-S equations are used (2-d case of Eq.1) as the example to demonstrate the conflict in the co-optimization process. The PDE and data loss can be written in a 2-dimensional case as:

$$\begin{aligned} L_{PDE} &= \frac{1}{M} \left\| \frac{\partial u_i}{\partial t} + u_j \frac{\partial u_i}{\partial x_j} + \frac{1}{\rho} \frac{\partial p}{\partial x_i} - \nu \frac{\partial^2 u_i}{\partial x_j^2} \right\|_2 + \frac{1}{M} \left\| \frac{\partial u_i}{\partial x_i} \right\|_2 \\ &= \frac{1}{M} \left\| \frac{\partial u}{\partial t} + (u \frac{\partial u}{\partial x} + v \frac{\partial u}{\partial y}) + \frac{1}{\rho} \frac{\partial p}{\partial x} - \nu (\frac{\partial^2 u}{\partial x^2} + \frac{\partial^2 u}{\partial y^2}) \right\|_2 \\ &\quad + \frac{1}{M} \left\| \frac{\partial v}{\partial t} + (u \frac{\partial v}{\partial x} + v \frac{\partial v}{\partial y}) + \frac{1}{\rho} \frac{\partial p}{\partial y} - \nu (\frac{\partial^2 v}{\partial x^2} + \frac{\partial^2 v}{\partial y^2}) \right\|_2 \\ &\quad + \frac{1}{M} \left\| \frac{\partial u}{\partial x} + \frac{\partial v}{\partial y} \right\|_2 \\ L_{data} &= \frac{1}{N} \left\| \mathbf{y} - \hat{\mathbf{y}} \right\|_2 \end{aligned} \quad (6)$$

where $\mathbf{x} = (t, x_i) = (t, x, y)$ and $\mathbf{y} = (u_i, p) = (u, v, p)$ represent the input and output of NN respectively. M and N are the number of collocation points and observation points.

Since the discrete data also contains the differential information, observation data adds the embedding PDE information to the training process. When the data is sufficient and clean (as in the situation in Fig.2.c), the observation data is consistent with PDE constraints. The PDE can be represented by observation data as Prop.1.

Proposition. 1. The no conflict condition. *When the number and distribution of observation data are sufficient to describe PDE solutions and the observation data is accurate, discrete data satisfy PDE constraints. The conflict can be represented as the following equation (the difference between residual*

form of PDE and observation data). In this condition, the conflict is close to 0.

$$PDE(\mathbf{y}) = \frac{u_i^{t+1} - u_i^t}{\Delta t} + u_j \frac{u_i^{x_j+1} - u_i^{x_j}}{\Delta x_j} + \frac{1}{\rho} \frac{p^{x_i+1} - p^{x_i}}{\Delta x_i} - \nu \frac{u_i^{x_j+1} - 2u_i^{x_j} + u_i^{x_j-1}}{\Delta x_j^2} \approx 0$$

where $PDE(\mathbf{y})$ is the residual form value of given PDE. The variables in Prop.1 all from the observation data.

When the data is noisy (like the restoration in Fig.2.b2), the observation data also contains noisy information about embedding solution distribution (given in Prop.2). That is, even if the NN can fit the observation data, the PDE constraint cannot be satisfied.

Proposition. 2. The conflict caused by the noise in observation data. *When the noisy data is used in the NN training, the conflict between PDE and data constraints occurs. The noisy data can't represent PDE well, which makes the residual form value of PDE with noisy data larger than that with accurate data. When the NN tries to fit the value, the PDE constraint loss will increase, which causes the difficulties in co-optimization.*

$$PDE(\mathbf{y} + \epsilon) = \frac{(u_i^{t+1} + \epsilon) - (u_i^t + \epsilon)}{\Delta t} + (u_j + \epsilon) \frac{(u_i^{x_j+1} + \epsilon) - (u_i^{x_j} + \epsilon)}{\Delta x_j} + \frac{1}{\rho} \frac{(p^{x_i+1} + \epsilon) - (p^{x_i} + \epsilon)}{\Delta x_i} - \nu \frac{(u_i^{x_j+1} + \epsilon) - 2(u_i^{x_j} + \epsilon) + (u_i^{x_j-1} + \epsilon)}{\Delta x_j^2}$$

thus $\|PDE(\mathbf{y} + \epsilon)\|_2 \geq \|PDE(\mathbf{y})\|_2 \approx 0$, $\epsilon \sim N(0, \sigma)$

When the observation data is sparse and incomplete, the contained information is not enough to help NN to learn the large-scale distribution of solutions (Prop.3). Under this condition, NN needs to learn the PDE relationship at collocation points without reference. The search space of optimization will expand significantly from the standpoint of the gradient descent process. Although the observation data is error-free and the actual PDE calculation happens at the collocation points, the optimization directions of PDE and data loss (like partial derivative terms in Eq.5) are always in conflict.

Proposition. 3. The conflict caused by the missing of observation data. *When the training data is sparse sampled, the distribution information in observation data is not enough. NN need to find the missing value by PDE constraint, thus cause the potential conflict in the optimization process. Theoretically, the $PDE(\mathbf{y}_{sparse})$ can be closed to 0, but finding the correct solution is similar to solving PDE with no observation data.*

$$PDE(\mathbf{y}_{sparse}) = \frac{u_i^{T+1} - u_i^T}{\Delta T} + u_j \frac{u_i^{X_j+1} - u_i^{X_j}}{\Delta X_j} + \frac{1}{\rho} \frac{p^{X_i+1} - p^{X_i}}{\Delta X_i} - \nu \frac{u_i^{X_j+1} - 2u_i^{X_j} + u_i^{X_j-1}}{\Delta X_j^2}$$

where $\Delta T, \Delta X_i \gg \Delta t, \Delta x_i$

Due to the existence of the inevitable conflict, the optimization direction will be unclear. The conflict slows the effective gradient descent and eventually results in an insurmountable local optimum.

2.2 The inspiration from LES

In order to model the noisy and sparse data better, it is necessary to find a way to overcome the conflict. When calculating the differential terms, the influence of noise or sparsity should be minimized as much as possible. Similar challenges will also be faced in numerical simulation, thus we can refer to existing methods to overcome the challenges. The filters in the numerical method give us inspiration.

In the numerical simulation method, solving the complex equations always means more computational cost in order to maintain accuracy. In the computational fluid dynamics (CFD) field, as the Reynolds number increases, the flow tends to be unsteady and disorderly. Since the simulation range is from the domain scale to the smallest dissipation scale, the computational requirement grows at Re^3 rate[35]. Under the large Reynolds number condition, direct simulation is unaffordable.

The large eddy simulation (LES)[34] method provides a way to reduce the computational cost as well as guarantee the accuracy. In LES, the computational scale is larger than in direct numerical simulation.

The small-scale information in LES is replaced and characterized by the artificially designed subgrid-scale model. Conclusively, the LES method greatly reduces the computational cost and maintains the quality of the solution. The solution of LES is equal to the solution of the filtered N-S equations (Eq.7).

$$\frac{\partial \bar{u}_i}{\partial t} + \frac{\partial \bar{u}_i \bar{u}_j}{\partial x_j} = -\frac{1}{\rho} \frac{\partial \bar{p}}{\partial x_i} + \nu \frac{\partial^2 \bar{u}_i}{\partial x_j^2} \quad (7)$$

where $\bar{u}_i, \bar{u}_j, \bar{p}$ represent the filtered variables in original equation (i.e., Eq.1)

In the problem of solving PDE via NN, the complex solutions also cause bias and insufficiency of observation data which intensify the conflicts in section 2.1. Therefore, it is intuitive to find a surrogate constraint to make the NN ignore the small-scale conflict and focus on the large-scale optimization. Although it is intuitive to do the filter operation on the observation data (i.e., the average pooling or the Gaussian filter in the data pre-processing), the operation like pooling loses information in the observation data and be hard to implement when the observation data is sparse and randomly distributed. Inspired by LES, we designed a method which filters the NN output in post-processing and rebuilds the governing equations (N-S equations as the example in Eq.8) rather than simply filter the observation data. The new PDE loss defined by the new governing equation acts as a surrogate constraint for the original PDE loss in the training, which is named as ‘filtered partial differential equations’ (FPDE) loss.

$$FPDE(\bar{\mathbf{y}}) = \frac{\partial \bar{u}_i}{\partial t} + \frac{\partial \bar{u}_i \bar{u}_j}{\partial x_j} + \frac{1}{\rho} \frac{\partial \bar{p}}{\partial x_i} - \nu \frac{\partial^2 \bar{u}_i}{\partial x_j^2} \quad (8)$$

3 Methodology

To deploy the filter before the PDE calculation, a new intermediate layer is designed to connect the normal NN outputs and the differentiation module. In the context of deep learning, the proposed layer can be viewed as a new activation layer, which helps the following calculation smooth the small-scale oscillations. In addition to the theoretical analysis (section 3.2), three experiments are conducted to verify the proposed method. The sparsely sampled simulation data with artificial noise is used to evaluate the improvement quantitatively, and finally test with the real cell migration and arterial flow data.

3.1 Deploying filter after NN inference

The filter operation in physics always implies the constraint of spatial resolution, which can be defined as the convolutional integral in Eq.9. In this integral equation, G is the filter, and ϕ is the objective function.

$$\bar{\phi}(x, t) = \int_{-\infty}^{\infty} \phi(y, t) G(x - y) dy \quad (9)$$

The classic physical isotropic spatial filters[36] (G in Eq.9) and its Fourier transformation in spectral space is shown in Fig.4. All filters satisfy the normalization condition to maintain the constants, and the kernel size of filters is represented as Δ . In this paper, all the experiments used the Gaussian kernel. The subsequent experiment verified that the FPDE results are not significantly affected by the type of filter. For details and results of the experiment, please refer to Appendix.A.

In the context of the computer version, the filter operation on data is usually called down sampling. When the filter is applied to the PDE calculation, it can be viewed as a new layer in the NN and builds the bridge between the ‘fully connected layer’ and ‘auto differentiation’ (shown in Fig.5).

The major difference between the regular model and the FPDE model is the calculation of PDE. A multi-layer fully connected network is used as the body. The inputs of NN are the coordinates x and the time t . The unknown variables in PDE are the NN outputs (N-S equations as example in Fig.5). Fig.5.b is the conventional calculating process of the PDE loss, which gets the differential terms with NN outputs directly via auto differentiation. The improvements in FPDE are shown in Fig.5.c: (1) In the orange box, the cross-terms in the N-S equations are calculated before the filter operation. The cross-terms are necessary since the filter operation does not satisfy the associative property of multiplication. (2) The proposed filter, or the defined new activation layer, is shown in the green box. Benefiting from the

x

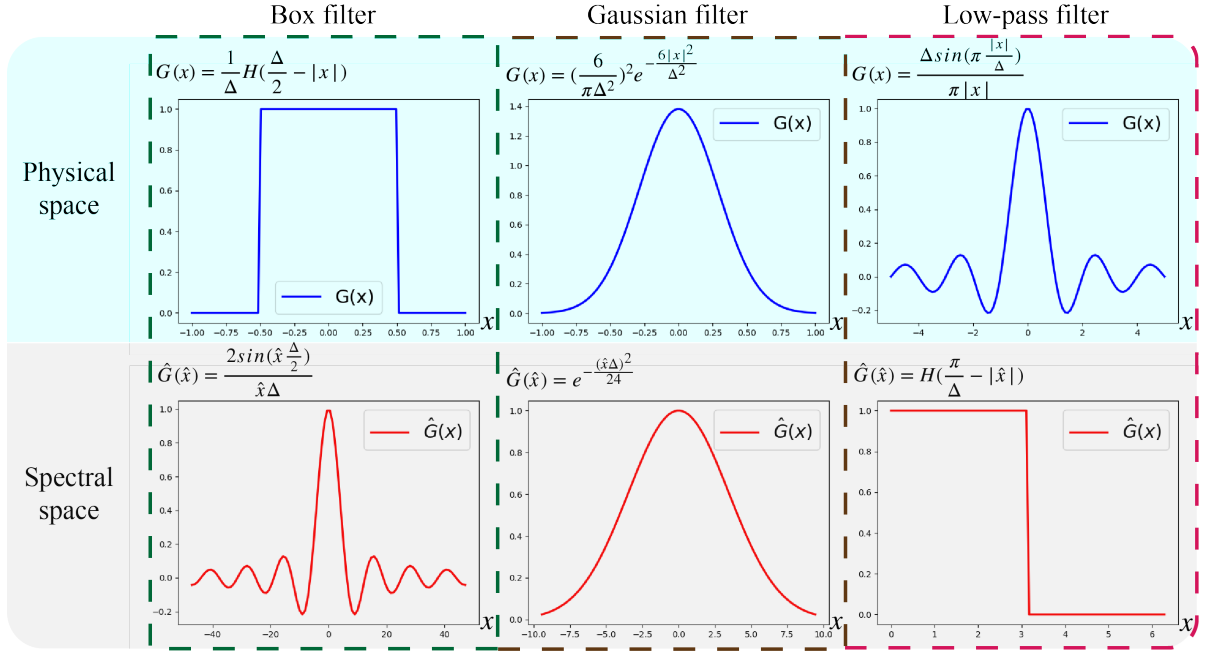


Fig. 4. The classic filters in physical and spectral space. The most common Gaussian weight filter kernel will be used in subsequent experiments.

mesh-free feature of NN, the gridded outputs for the filter operation can be obtained. The u is filtered to \bar{u} by the Gaussian kernel, and the differential terms are calculated on the filtered outputs.

The details of the training process for FPDE and the conventional PDE model can be summarized in Algorithm.1.

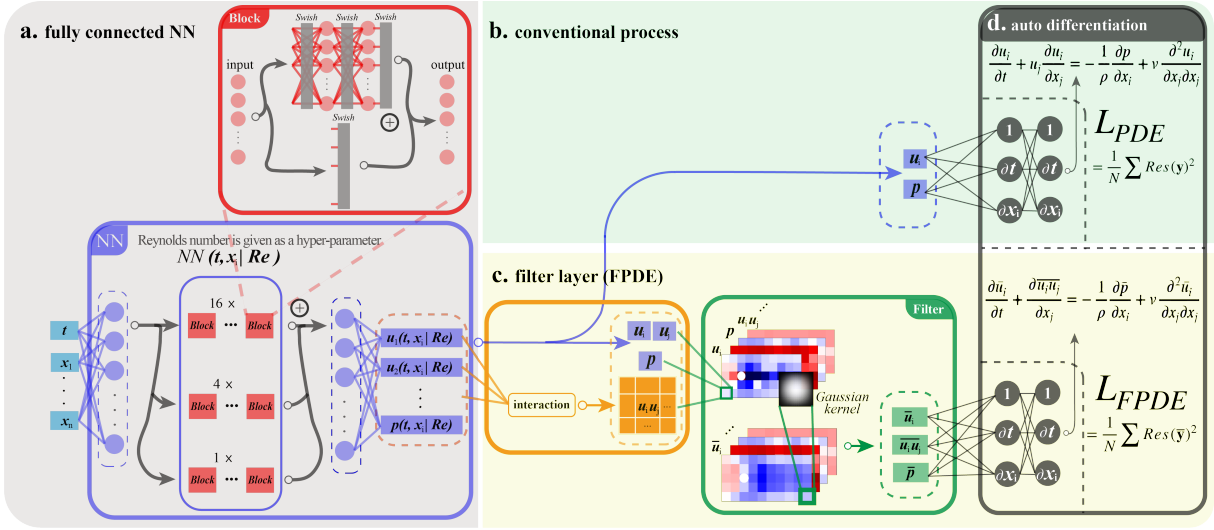


Fig. 5. The physics-informed training framework and the proposed FPDE method. The example of solving the N-S equation governed problem. (a) The fully connected neural network. A NN with multiple residual connections is used to model the observation. (b) The conventional PDE loss calculation process, which uses NN outputs in differentiation directly. (c) The improved framework in the PDE loss calculation iteration. The orange part is used to calculate the cross-terms in the equations; the green part is used to filter all variables. The PDEs are calculated with filtered variables instead. (d) The auto differentiation part. Derivatives are automatically generated from the computational graph.

Algorithm 1 FPDE and PDE training process (2-d NS equation as an example).

Input: Observation points $(x, y, t) \rightarrow (u, v, p)$; Collocation points $(x_{col}, y_{col}, t_{col})$.

Constraint: 2-d N-S equations; Initial condition (IC); Boundary condition (BC).

Loss: Mean Squared Error (MSE) loss

Repeat:

Step 1. Data loss: for (x, y, t) in observation data

1.1. Get NN output $(\hat{u}, \hat{v}, \hat{p})$ by forward propagation.

1.2. Calculate data loss $MSE((u, v, p), (\hat{u}, \hat{v}, \hat{p}))$.

Step 2. FPDE / PDE loss: for $(x_{col}, y_{col}, t_{col})$ in collocation points

2.1. Get NN output $(\hat{u}_{col}, \hat{v}_{col}, \hat{p}_{col})$ by forward propagation.

FPDE:

2.2. Get the gridded outputs to the 2-d tensor.

2.3. Filter the 2-d tensor (convolution with Gaussian kernel, i.e., $\bar{u} = \frac{1}{\sum \omega_i} \sum_{i=1}^n \omega_i u_i$, ω_i is the weight in kernel), get the filtered $(\bar{u}_{col}, \bar{v}_{col}, \bar{p}_{col})$.

2.4. Calculate the differential terms $\frac{\partial \bar{u}_{col}}{\partial t} \dots$, etc

2.5. Calculate FPDE loss of the residual form equations.

PDE:

2.2. Calculate the differential terms $\frac{\partial u_{col}}{\partial t} \dots$, etc

2.3. Calculate PDE loss of the residual form equations.

Step 3. IC / BC loss: for $(u_{ICBC}, v_{ICBC}, p_{ICBC})$ generated by initial / boundary condition

3.1. Get NN output $(\hat{u}_{ICBC}, \hat{v}_{ICBC}, \hat{p}_{ICBC})$ by forward propagation.

3.2. Calculate IC/BC loss $MSE((u, v, p), (\hat{u}_{ICBC}, \hat{v}_{ICBC}, \hat{p}_{ICBC}))$.

Step 4. Optimization:

4.1. Calculate total loss = data loss + equation loss + IC/BC loss

4.2. Backward propagation and update NN parameters.

Until the training loss has converged.

The algorithm 1 is the description of Fig.5. Algorithm 1 compares the difference between the FPDE and classical model more clearly. In both models, the form of the governing equations, initial and boundary conditions, and observation points are completely the same. The only difference is the FPDE intermediate layer between the forward propagation and auto differentiation parts (i.e., the orange and

green boxes in Fig.5.b). In order to calculate the filtered PDE, the obtained NN inference outputs need to be gridded. The gridded outputs (i.e., $(\hat{u}_{col}, \hat{v}_{col}, \hat{p}_{col})$, 2-d case) are filtered by the given kernel at step 2.3. The filtered variables (i.e., $(\bar{u}_{col}, \bar{v}_{col}, \bar{p}_{col})$) are pushed into the auto differentiation part to calculate the differential terms. In the whole FPDE process, the most critical steps are 2.2 and 2.3. Benefit from the mesh-less feature of NN, it is simple to get the gridded neighbors of given points (i.e., the $NN(x_{col} \pm \Delta x, y_{col} \pm \Delta y, t_{col})$) and obtain the filtered results.

In general, the calculation of FPDE loss can be divided into two steps: calculating cross-terms and filtering. FPDE is transparent for NN architectures and forms of governing equations due to its simplicity. That means FPDE can be applied to most NN architectures and different equations, not just the given example cases.

3.2 Theoretical improvements of filter

The filtered partial differential equations (FPDE) method is deployed as the surrogate constraint of the original PDE loss. The FPDE constraint helps the optimization process of NN and improves the model's performance in the 'inference-filtering-optimization' process. The examples are given to demonstrate these improvements.

Training with noisy data (like the restoration in Fig.2.b2), the FPDE is more accurate because of the anti-noise ability of the filter operation. As the basic filter with the Gaussian kernel, the filtered output has a smaller variance than the original output, according to the Chebyshev's inequality[37]. The normally distributed noise $N(0, \sigma)$, as the most common unbiased noise, is chosen to show that the FPDE loss value is closer to the noise-free value than the original loss value (Eq.10).

$$\begin{aligned}
 FPDE(\bar{\mathbf{y}} + \bar{\epsilon}) &= \frac{(\overline{u_i^{t+1}} + \bar{\epsilon}) - (\overline{u_i^t} + \bar{\epsilon})}{\Delta t} + (\overline{u_j} + \bar{\epsilon}) \frac{(\overline{u_i^{x_j+1}} + \bar{\epsilon}) - (\overline{u_i^{x_j}} + \bar{\epsilon})}{\Delta x_j} \\
 &+ \frac{1}{\rho} \frac{(\overline{p^{x_i+1}} + \bar{\epsilon}) - (\overline{p^{x_i}} + \bar{\epsilon})}{\Delta x_i} - \nu \frac{(\overline{u_i^{x_j+1}} + \bar{\epsilon}) - 2(\overline{u_i^{x_j}} + \bar{\epsilon}) + (\overline{u_i^{x_j-1}} + \bar{\epsilon})}{\Delta x_j^2} \quad (10) \\
 \epsilon &\sim N(0, \sigma), \quad \bar{\epsilon} \sim N\left(0, \frac{\sigma \sum \omega_i^2}{\sum \omega_i}\right), \quad \omega_i = \frac{1}{\sqrt{2\pi}} \exp\left(-\frac{x^2}{2}\right)
 \end{aligned}$$

where ϵ and $\bar{\epsilon}$ represent the noise and filtered noise, ω_i represents the weight in filter. With the Gaussian kernel as the filter operator, the variance of noise decreases at the rate of n^{-1} (n is the size of given Gaussian kernel). This indicates that just a small kernel can greatly reduce the interference of noise.

Noisy observation data can cause NN to give inaccurate predictions. The influence and tendency of noise are shown in Fig.6.a, the data loss leads the NN output close to the noisy observation data in each iteration. Then, the NN output, which is influenced by the noisy data, will bias the calculation of PDE. In Fig.6.b, a simple example shows that the filtered output (blue star) is closer to the real solution, the filtered star point provides the correct derivative to help NN resist the noise. In a conventional PDE model, the outputs (blue dots) are influenced by the noise (pink line), and can not provide the correct derivatives. In conclusion, the filtering operation reduces the value of noise. The FPDE is more robust to noisy data, provides better optimization direction, and is capable of continuously correcting the NN outputs in the training process.

The improvement of training with sparse data can be regarded as the inverse application of the FPDE advantages above. In Eq.10, the difference in the optimization direction between data and PDE loss is reduced by filtering, and the NN isn't restricted by the coupling of two losses. In section 2.1, we demonstrate that the conflict arises from low-quality data. When using sparse data for training, the FPDE method was found to continue to optimize under greater conflict. In the view of co-optimization, the reduction of conflict can be regarded as the decoupling of the data and PDE loss inversely.

Mathematically, the decoupling can be explained by the increase in degrees of freedom (df). In the comparison of the FPDE model and the conventional PDE model with sparse data, the simple residual form of the PDE loss constrains the solution directly, while the FPDE constrains the filtered 'mean' solution, increasing the df of the problem (Eq.11). Compared with the original problem, the FPDE governed problem has more variables that can be learned freely. From this perspective, FPDE partially

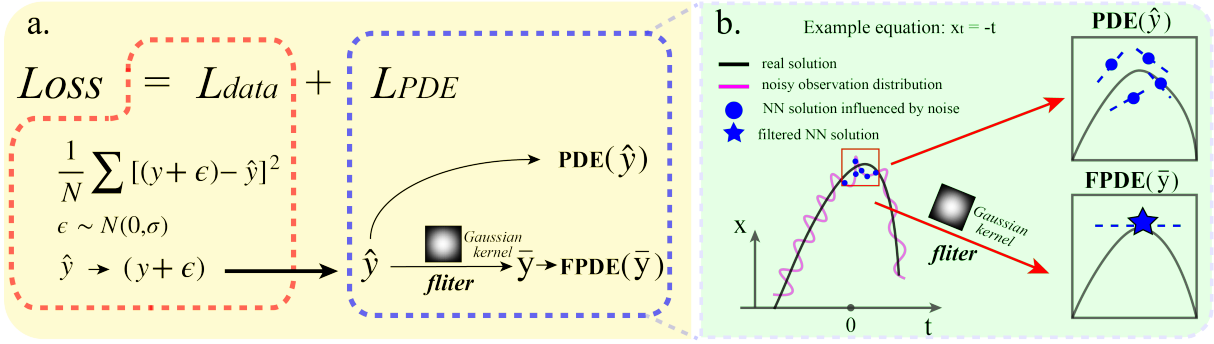


Fig. 6. The mechanism of the FPDE method for processing noisy data. (a) Though the noisy data doesn't directly participate in the PDE loss calculation, it still affects the PDE loss by changing the NN output from the previous iteration. (b) The filtered NN outputs reduce the noise, making PDE calculations more robust and accurate.

decouples the PDE loss and data loss in the training process.

$$\begin{aligned}
 FPDE(\overline{\mathbf{y}_{sparse}}) &= \frac{\overline{u_i^{T+1}} - \overline{u_i^T}}{\Delta T} + \overline{u_j} \frac{\overline{u_i^{X_j+1}} - \overline{u_i^{X_j}}}{\Delta X_j} + \frac{1}{\rho} \frac{\overline{p^{X_i+1}} - \overline{p^{X_i}}}{\Delta X_i} - \nu \frac{\overline{u_i^{X_j+1}} - 2\overline{u_i^{X_j}} + \overline{u_i^{X_j-1}}}{\Delta X_j^2} \\
 \overline{u} &= \frac{1}{\sum \omega_i} \sum_{i=1}^n \omega_i u_i, \quad \omega_i = \frac{1}{\sqrt{2\pi}} \exp\left(-\frac{x^2}{2}\right) \\
 \text{for } PDE(\mathbf{y}_{sparse}), \quad df_{sparse} &= k - m = 0 \\
 \text{for } FPDE(\overline{\mathbf{y}_{sparse}}), \quad df_{\overline{sparse}} &= n * k - m \geq 0
 \end{aligned} \tag{11}$$

where df_{sparse} and $df_{\overline{sparse}}$ represent the degree of freedom in the original and filtered equations respectively. k and m represent the number of variables in equations and the number of equations. n is the filter size, which increases the number of variables ($n * k$) in the equations.

The FPDE's co-optimization improvements can be intuitively demonstrated from the decoupling perspective. Decoupling is a common method to optimize complex systems. It simplifies the description of problems using less relevant variables and allows the optimization to be less affected by relevance. In the Knapsack problem in dynamic programming, we can easily write the state transition equation $S_{t+1} = f(S_t)$ and find the optimal solution because the optimization process is satisfied the Markov property[38], which means no coupling exist in the optimization. If there is a coupling relationship between the current state S_t and the next state S_{t+1} , finding a global optimum becomes a non-convex problem.

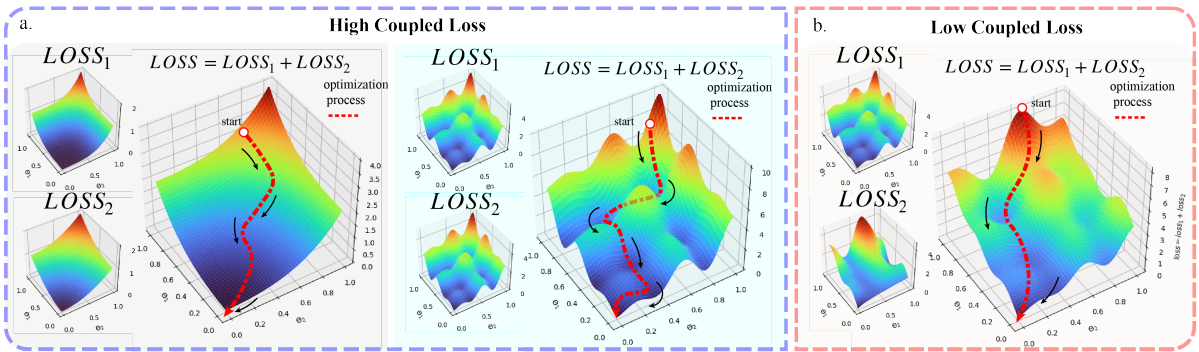


Fig. 7. The impact of coupling on optimization. (a) The superposition of two highly coupled losses enlarges the local optimum and makes optimization harder. The simple case (left) is not affected much, while the optimization of the complex case (right) becomes more difficult. (b) Superposition of two more irrelevant losses have shallower local optimum than part a.

Coupled variables can affect each other, make the optimization difficult. The NN is a complex system, co-optimization between PDE and data loss is also affected by the coupling. In the co-optimization of

PDE and data loss, the improvement of decoupling can be illustrated specifically in Fig.7. Assume exist Loss 1 and Loss 2, and the lowest point (i.e., the origin point) of the surface represents the global optimum. Fig.7.a shows two optimization processes (red line) for two highly coupled losses. In the right complex case of Fig.7.a, coupling has a greater impact on the local optimum than it does in the left simple case. Two highly coupled losses allow the optimization to be easily trapped. The low coupled losses are shown in Fig.7.b, indicating that the local optimum of Loss 2 is smoothed by the irrelevant Loss 1 in total loss.

In conclusion, the conflict is used to demonstrate the difficulty in co-optimization process and the proposed FPDE method can help NN overcome the conflict better. The FPDE surrogate constraint decreases the coupling between the PDE and data loss, making it easier for NN to jump out of the local optimum. Under the noisy observation condition, the FPDE is more accurate and is capable of continually correcting the NN output.

3.3 Design of experiments

Three experiments—the cylinder flow, cell migration, and artery flow—are used to demonstrate the performance of FPDE on sparse and noisy data. In the cylinder flow case, the improvements of FPDE with simulation data is verified quantitatively; in the cell migration case, we evaluate the FPDE’s ability to correct real data when equations have missing coefficients; in the arterial flow case, we evaluate the performance of FPDE with inconsistent equations and observation data.

3.3.1 Simulation data of cylinder flow

To verify the improvement of FPDE under sparse and noisy conditions, sparsely sampled simulation data and add artificial noise for training. In the experiment, the sampling ratio and noise level can be controlled to quantitatively demonstrate the improvement effect of FPDE.

For details of cylinder flow, data sources, and pre-processing methods, please refer to Appendix.B. The Fig.8 below is an overview of the simulation data.

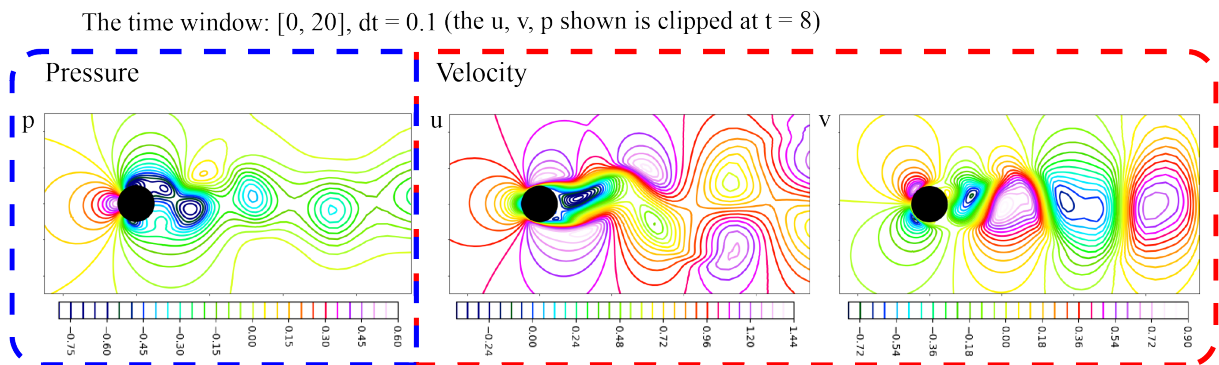


Fig. 8. The numerical simulation data of the cylinder flow problem. The training data is sampled from the original data and contaminated with noise. Similar to the boundary condition, the black circle is the cylinder wall.

Finally, experiments are conducted in two groups to evaluate the effects of sparsity and noise. The details of the two groups of datasets are presented in Table 1. For each experiment, the FPDE and the baseline model are trained in parallel to show improvements. The processes of data sampling and adding noise are also described in Appendix.B.

Table. 1. Summary of two groups of data. These groups of data are used to train the FPDE and conventional PDE models and validate their flow restoration abilities under sparse and noisy conditions.

The evaluation criteria is defined in Eq.12. The conventional PDE model and FPDE model are trained

| Base data | Group and Data overview | | | | | |
|------------------------|---|------------------|------------------|-------------------|-------------------|-------------------|
| | Group 1: sparse data sampled by different sampling ratio | | | | | |
| full size | 2^{-8} | 2^{-10} | 2^{-12} | 2^{-13} | 2^{-14} | 2^{-16} |
| | Group 2: noisy data generated by different noisy standard deviation | | | | | |
| 2^{-10} sampled data | $25\% \cdot std$ | $50\% \cdot std$ | $75\% \cdot std$ | $100\% \cdot std$ | $125\% \cdot std$ | $150\% \cdot std$ |

and tested on the same dataset.

$$\begin{aligned}
Loss &= \frac{1}{N} \|\mathbf{y} - \hat{\mathbf{y}}\|_2 + \frac{1}{M} \left(\sum_{i=1}^3 \|e_i\|_2 \right) + \frac{1}{W} \left\| \frac{\partial^k \mathbf{y}_{IC/BC}}{\partial \mathbf{x}_{IC/BC}^k} - \frac{\partial^k \hat{\mathbf{y}}_{IC/BC}}{\partial \mathbf{x}_{IC/BC}^k} \right\| \\
e_1 &= \frac{\partial u}{\partial t} + \left(u \frac{\partial u}{\partial x} + v \frac{\partial u}{\partial y} \right) + \frac{1}{\rho} \frac{\partial p}{\partial x} - \nu \left(\frac{\partial^2 u}{\partial x^2} + \frac{\partial^2 u}{\partial y^2} \right) \\
e_2 &= \frac{\partial v}{\partial t} + \left(u \frac{\partial v}{\partial x} + v \frac{\partial v}{\partial y} \right) + \frac{1}{\rho} \frac{\partial p}{\partial y} - \nu \left(\frac{\partial^2 v}{\partial x^2} + \frac{\partial^2 v}{\partial y^2} \right) \\
e_3 &= \frac{\partial u}{\partial x} + \frac{\partial v}{\partial y}
\end{aligned} \tag{12}$$

where N, M, W represent the numbers of observation, collocation and IC/BC points in one iteration, respectively. e_1, e_2, e_3 represent the values of residual form PDE (N-S equations as example). $\frac{\partial^k}{\partial \mathbf{x}_{IC/BC}^k}$ represents the paradigm of boundary conditions in different task (e.g., $k=0 / 1$ means the Dirichlet / Neumann boundary condition).

3.3.2 Measurement data of cell migration

In this experiment, the real-world measurement data is used to demonstrate the improvement of FPDE in real-world situations. Generally, there are two difficulties when using real data in this experiment. The first difficulty is the high noise in the observation data. In the experiments, the measurement data is mainly obtained by sensors or manual measurements, which means the data is always noisy and sparse. When the measurement data is used as observation points in physics-informed framework, it leads to conflict between data distribution and theoretical equation. The cell number C has high noise because the experimental data is automatically collected by the CV algorithm. The second difficulty in this experiment is the missing coefficients in the equations. Since some coefficients of the equation are unknown, NN predicts those segments without collocation points.

The cell migration data in reproducibility of scratch assays is affected by the initial cell density in the given scratch[39]. It shows the relationship of cell distribution in scratch assays with time, space, and initial cell density. The data shows that when a scratch occurs, cells migrate to repair the scratch. Existing theories often use the Fisher-Kolmogorov model to describe the process of collective cell spreading, which can be written as:

$$\frac{\partial C}{\partial t} = D \frac{\partial^2 C}{\partial x^2} + \lambda C \left[1 - \frac{C}{K} \right] \tag{13}$$

where the dependent variable C represents the cell concentration. K, λ and D represent the carrying capacity density, the cell diffusivity and the cell proliferation rate respectively. In this experiment, K, λ and D can be viewed as the coefficients decided by initial cell density (n). Because this is a variable coefficient equation, it cannot calculate the unknown PDE at any collocation points. In this paper's experiment, the coefficients in $n = 14,000$ and $n = 20,000$ are known. The aim is to model the $n \in (14,000, 20,000)$ interval data through the FPDE training.

The Fig.9 below is a schematic diagram of the cell migration experiment. For more details on the experiment, coefficients, and dataset distribution, please refer to Appendix.C.

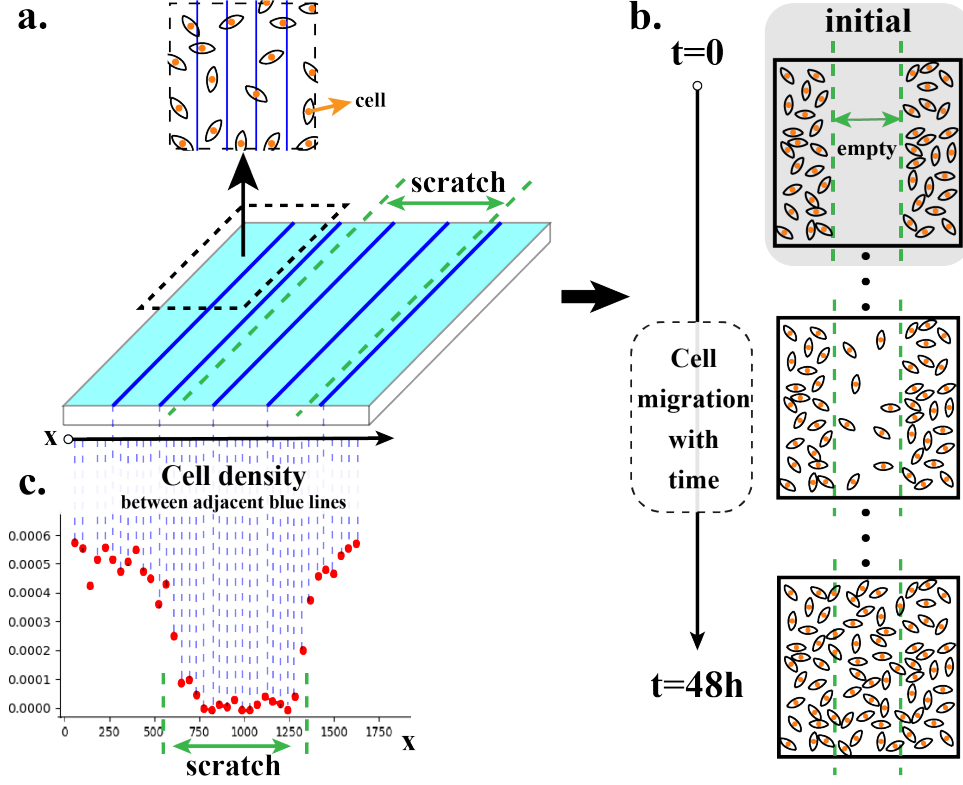


Fig. 9. The experiment of cell migration and data collection. (a) The square petri and counting method of blue lines. (b) Cells fill in the scratch by migrating. (c) Measurement data distribution.

In short, the NN models the mapping relationship ‘ $NN(t, x, n) \rightarrow C$ ’. And the final loss function in Eq.4 can be written as follows (Eq.14). When it comes to the calculation of FPDE, the variable C is filtered first and calculated in the same form as Eq.14. The conventional PDE model and the FPDE model are trained until converged and tested on the same dataset.

$$\begin{aligned}
 Loss &= \frac{1}{N} \|C - \hat{C}\|_2 + \frac{1}{M} (\|e\|_2) + \frac{1}{W} \left\| \frac{\partial^k \mathbf{y}_{IC/BC}}{\partial \mathbf{x}_{IC/BC}^k} - \frac{\partial^k \hat{\mathbf{y}}_{IC/BC}}{\partial \mathbf{x}_{IC/BC}^k} \right\| \\
 e &= \frac{\partial C}{\partial t} - 530.39 \frac{\partial^2 C}{\partial x^2} - 0.066C + 46.42C^2, \text{ if } n = 14,000 \\
 e &= \frac{\partial C}{\partial t} - 982.26 \frac{\partial^2 C}{\partial x^2} - 0.078C + 47.65C^2, \text{ if } n = 20,000 \\
 e &= 0, \text{ else}
 \end{aligned} \tag{14}$$

where N, M, W represent the numbers of observation, collocation and IC/BC points in one iteration, respectively. e is the residual form value of Eq.19. Because of the changing coefficients, e should be calculated according to three categories ($n = 14,000/20,000/else$).

3.3.3 Measurement data of arterial flow

When the equation is obtained through the ideal model, there are always big differences between the actual situation and the description of the equation. In this experiment, arterial blood flow measurements are used to compare the modeling results of FPDE and baseline with noisy data.

The data on arterial flow shows the velocity of blood when it flows through the arterial bifurcation [40]. The theoretical equations of velocity are shown in Eq.15. A is the cross-sectional area of the vessel, and u is the axial velocity. Similar to the N-S equations (Eq.1, ρ and p represent density and pressure, respectively), A_1 and u_1 are the cross-sectional area and velocity of the interface in the aorta. A_2, u_2 and A_3, u_3 are the area and velocity of the interface in two bifurcations. The physical relationship between

the aorta and two bifurcations is shown in Fig.10.a, the real-world vessel's shape is shown in Fig.10.b.

$$\frac{\partial A}{\partial t} = -\frac{\partial Au}{\partial x}, \quad \frac{\partial u}{\partial t} + u \frac{\partial u}{\partial x} = -\frac{1}{\rho} \frac{\partial p}{\partial x} \quad (15)$$

$$A_1 u_1 = A_2 u_2 + A_3 u_3, \quad p_1 + \frac{\rho}{2} u_1^2 = p_2 + \frac{\rho}{2} u_2^2 = p_3 + \frac{\rho}{2} u_3^2$$

An overview of the experiment is shown in the Fig.10. Notably, a multi-head neural network is used to fit different segments of vessels. Briefly, the aim is to train the NN with measurement data from only four observation points and model the entire blood vessel.

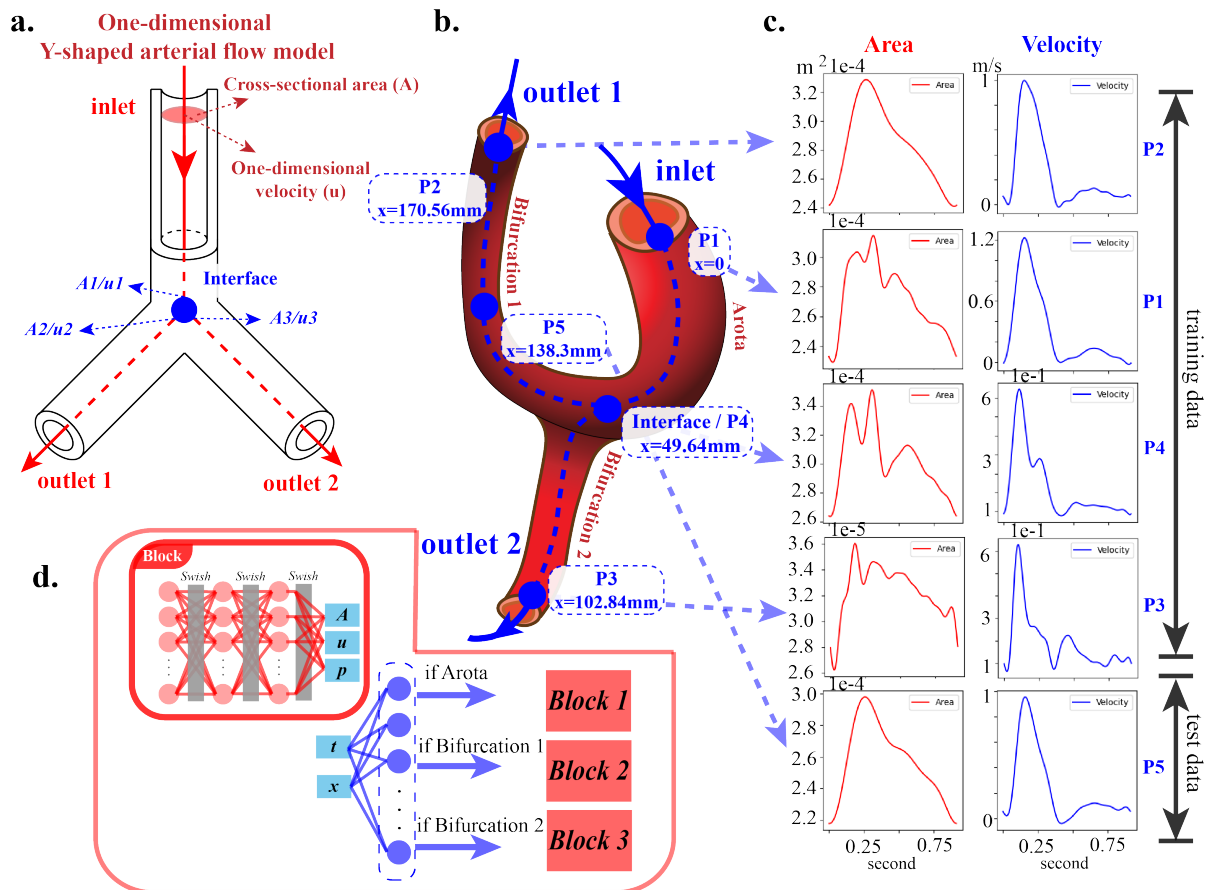


Fig. 10. The experiment of one-dimensional blood flow in the Y-shaped artery. (a) The theoretical model (including the definitions of A , A_i and *interface*). The Eq.15 used in the training are derived from this model. (b) The location of five measurement points and the schematic diagram of artery. (c) Overview of measurement data (area and velocity). (d) Multi-head NN to predict the velocity in different vessels.

Fig.10 shows the experiment of one-dimensional blood flow in the Y-shaped artery. Previous studies modeled the velocity at the bifurcation based on an idealized Y-shaped one-dimensional vessel (shown in Fig.10.a). The actual blood isn't ideal, thus the measurement data always can't fit the embedding distribution in Eq.15 well. The conflict raised in section 2.1 affects optimization a lot. In the real experiment measuring blood flow, the schematic diagram of an artery is shown Fig.10.b, with blood directions indicated by blue dotted lines. The data are measured at the five points, which are shown in Fig.10.b, and the measured variables (A , u) are shown in Fig.10.c. The in-vivo data is measured by the Magnetic Resonance Imaging (MRI) method in Machine learning in cardiovascular flows modeling[40]. All data (area and velocity) are measured within 850ms. Since the data is measured in an open vessel, the boundary condition is unknown in training.

In order to model the distribution ' $NN(t, x) \rightarrow (A, u, p)$ ' in three parts of vessel, we build a multi-head NN to predict the (A, u, p) in different parts separately (shown in Fig.10.d). NN is trained by the

data from three endpoints (points 1, 2, and 3) and the interface (point 4). The collocation points are sampled among the entire vessel as constraints. The data in point 5 is reserved for testing. During parallel training, baseline PDE is calculated directly. When calculating FPDE, the variables $y = (A, u, p)$ are filtered first and calculated in the same form as in Eq.16.

The final loss function in Eq.4 can be written as follows. Conventional PDE model and FPDE model are trained until converged and tested in same dataset.

$$\begin{aligned}
Loss &= \frac{1}{N} \|\mathbf{y} - \hat{\mathbf{y}}\|_2 + \frac{1}{M} \left(\sum_{i=1}^2 \|e_i\|_2 \right) + \frac{1}{W} \left(\sum_{i=1}^3 \|f_i\|_2 \right) \\
e_1 &= \frac{\partial A}{\partial t} + \frac{\partial Au}{\partial x}, \quad e_2 = \frac{\partial u}{\partial t} + u \frac{\partial u}{\partial x} + \frac{1}{\rho} \frac{\partial p}{\partial x} \\
f_1 &= A_1 u_1 - A_2 u_2 - A_3 u_3 \\
f_2 &= p_1 + \frac{\rho}{2} u_1^2 - p_2 - \frac{\rho}{2} u_2^2, \quad f_3 = p_1 + \frac{\rho}{2} u_1^2 - p_3 - \frac{\rho}{2} u_3^2
\end{aligned} \tag{16}$$

where N, M, W represent the numbers of observation, collocation and interface points in one iteration, respectively. e_1, e_2 represent the residual value of governing equations, f_1, f_2 represent the residual value of the interface constraints which constrain mass and energy conservation in interface.

4 Results

In order to verify the advantage of FPDE constraint over conventional PDE constraint, the performance of the corresponding models are compared in this section via multiple experiments. For comparison, the NN output, the residual map, and the converged losses are plotted. The experiment results prove the existence of conflict (demonstrate in section 2.1) and FPDE model can overcome the conflict better (demonstrate in section 3.2).

4.1 The comparison between FPDE and baseline model

4.1.1 Quantitative analysis of simulation data

In the sparse data experiment, 7 pairs of converged losses are shown in the histogram of Fig.11.a. The simulation data is used as the ground truth in this experiment. The x-axis of this histogram is the number of simulation data used in the training dataset, and the bar on the y-axis is the MSE on test data. The residuals between the ground truth and NN restored flow field are plotted above the loss bar, where the top is the FPDE and below is the baseline residual. According to the color map in the residual plot, a whiter color means a solution that is closer to the ground truth. In Fig.11.a, the residuals of FPDE are less than baseline generally. This improvement is consistent with the losses of histogram responses.

FPDE model has better performance under the sparse observation data (which is common in real-world scenarios). For example, under the 2^{-12} sampling ratio, the MSE of the converged FPDE model is only 18% of the baseline. On average, the MSE on the converged FPDE model is 82.1% less than the baseline model in these 7 sparse cases. However, since the data in this experiment is accurate and the observation data of the first 3 groups are enough in quantity, FPDE models make no improvements. In the magnified part in Fig.11.a, the first 3 pairs of losses are close to the complete and error-free condition (i.e., case in Fig.2.c). In terms of the conflict, Prop.1 demonstrates that there is nearly no conflict between PDE and data loss. But in real-world measurements, the data are always sparse, where FPDE models can perform better.

The Fig.11.b shows the typical outputs in the sparse experiment. The restoration task is similar to the pure equations solving task at the lowest sampling ratio. Using the 2^{-16} sampling ratio case as the example, the number of used simulation data points is only 91. To show the sparsity directly, the comparison between the sampled data and full-size data points is shown on the top of Fig.11.b. The direct NN outputs are shown for the comparison of two models. It is obvious that the PDE solution becomes more trivial (like the example in Fig.3.c). With the filter operation, FPDE model can learn the characteristic of fluid better.

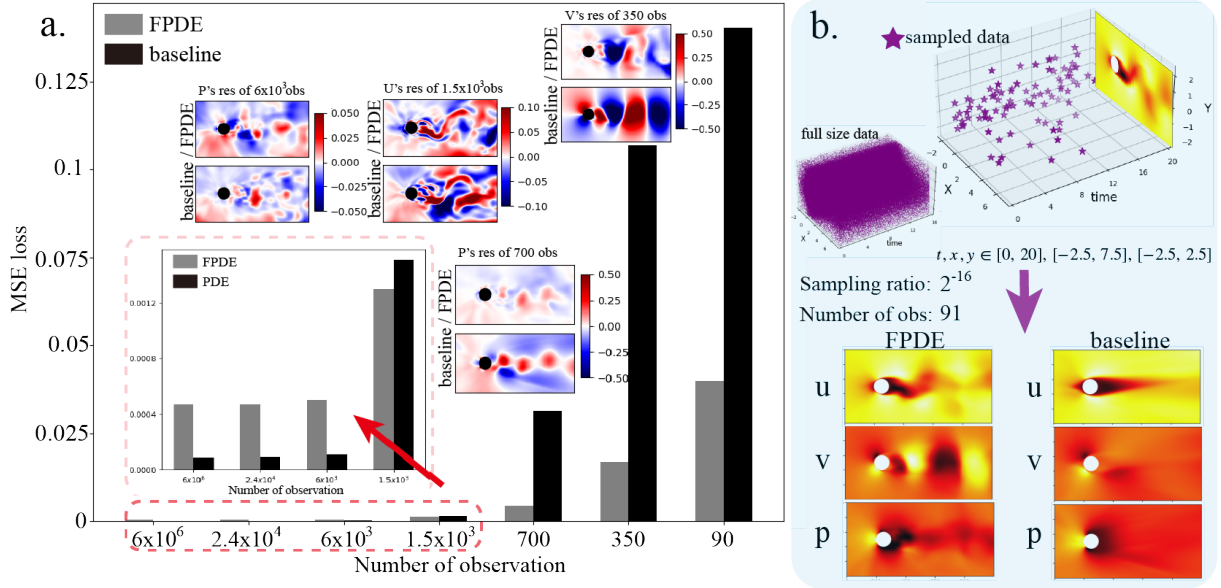


Fig. 11. The NN outputs and Mean Squared Error of the FPDE and baseline models. (a) The Mean Squared Error and the residual between the ground truth and output. This result shows the FPDE method works better with sparse observation. (b) A typical example with a 2^{-16} sampling ratio. The comparisons of NN outputs (u, v, p) are below.

In the noisy data experiment, the same kind of histogram and residuals are plotted in Fig.12.a. The conflict with noisy data is shown as Prop.2, which is accurately reflected by the losses in the histogram. Under the same noisy condition, the FPDE model always converged to a lower loss. Meanwhile, the residuals also show FPDE solutions are closer to the ground truth than the baseline model at all noise levels. The Fig.12.b is a typical example of this noisy group. Under the highest noisy level (150% std, additive white Gaussian noise), the generation of noisy data is shown on the top of Fig.12.b. Under the high-noise condition, the large-scale features disappear, and periodicity is difficult to reflect. But the FPDE model still shows better anti-noise ability than the baseline model. Only by varying the physics-informed function can the FPDE model significantly reduce the impact of outliers. On average, the MSE on the FPDE model is 62.6% less than the baseline model in these 7 noisy cases. Under the high-noise data (noisy level $> 125\%$), this number increases to 72.2%.

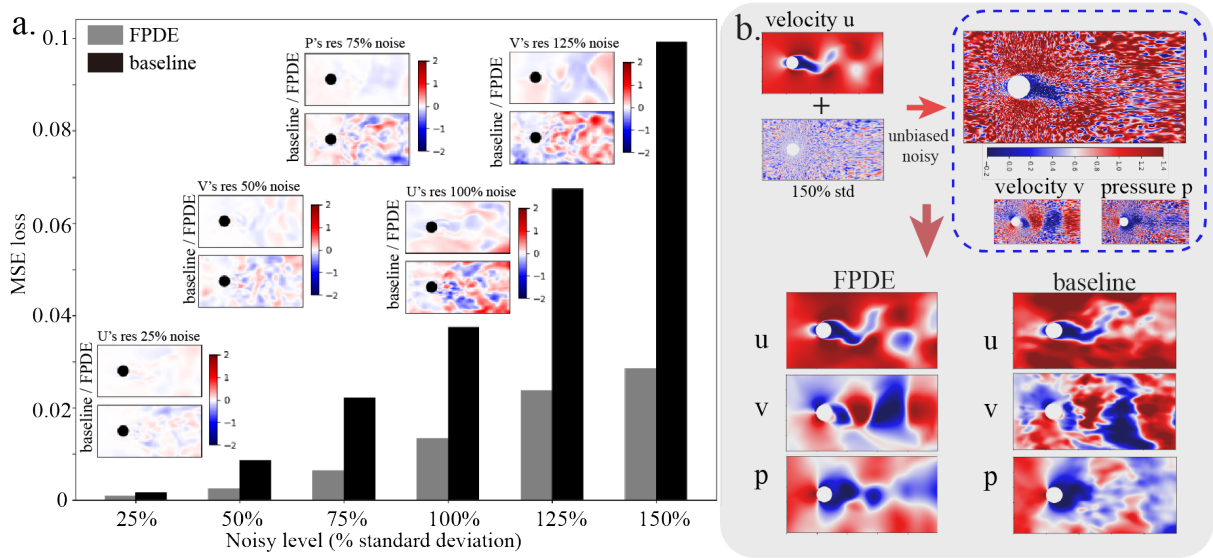


Fig. 12. The NN outputs and Mean Squared Error of the FPDE and baseline models under the noisy data condition. (a) The Mean Squared Error and residual plots. (b) The FPDE and PDE outputs under the additive white Gaussian noise with 150% standard deviation of observation data; the comparison of NN outputs is below.

4.1.2 Experiment results of real-world data

The data in the cell migration case is sparse and noisy. Additionally, due to fluctuating coefficients, the NN lacks collocation points to learn PDE on the test part. Both experiment results are shown in Fig.13 (initial cell number, $n = 16,000/18,000$). The predictions indicate the generalized ability of NN to learn the embedding distribution from given data. When confronted with an unknown equation, NN learns the embedding physical process (i.e., the general law of cell migration) through generalization from given equations. In Fig.13, the dots are the measurement data, and the lines are the NN predictions. Quantitatively, the MSE of normalized prediction decreased from 0.157 (baseline) to 0.121 (FPDE), a decrease of 22.9% when $n = 16,000$. When $n = 18,000$, this reduction increases to 42.9%, from 9.89×10^{-2} (baseline) to 5.64×10^{-2} (FPDE).

In the solutions of the baseline model, it is obvious that the high-noise initial data greatly affects the NN outputs. Outliers cause NN to make predictions that contradict physical laws. Although both models predict worse outcomes over time (e.g., the red lines at $t=48h$), FPDE model still has more robust results. The unreasonable solution comes because the outliers and the physical constraints cannot correct the prediction well. In the comparison, the FPDE model gave better predictions in the test part. The filter operation reduces the effect of outliers and makes NN learn the embedding distribution successfully.

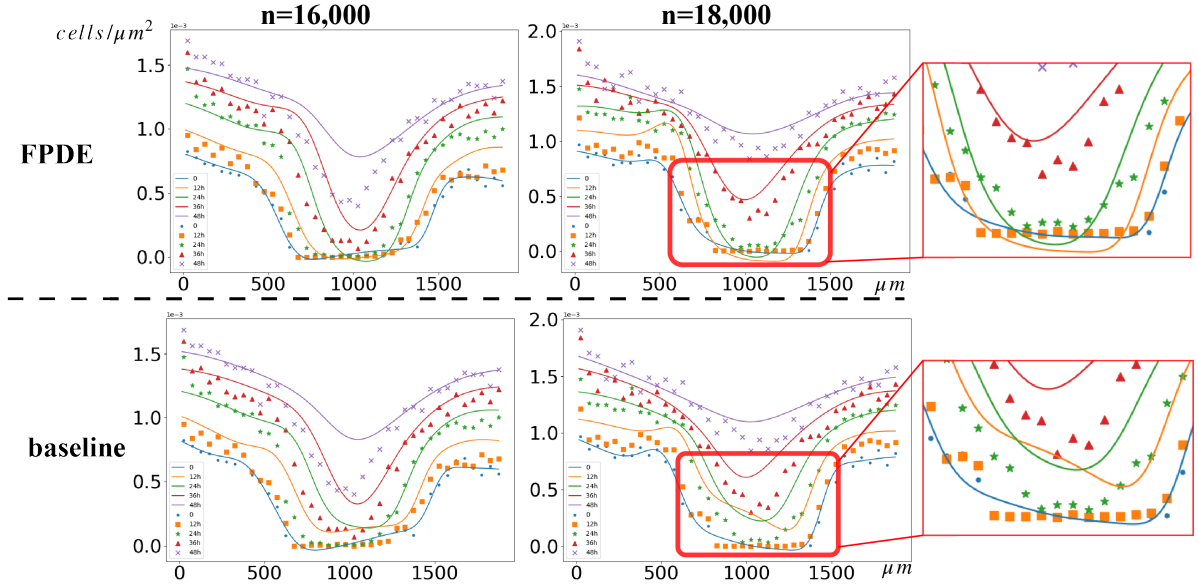


Fig. 13. Comparison in the cell migration test data (initial cell number = [16,000, 18,000]). Inside the red boxes, the difference between two outputs shows FPDE can overcome the influence of outliers better. This characteristic shows that the FPDE method has better modeling ability when faced with real, high-noise measurement data.

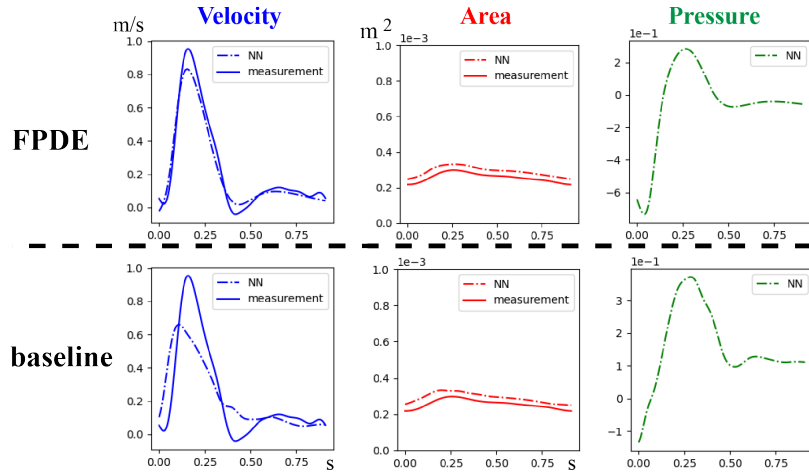


Fig. 14. Comparison in the arterial flow test data. The comparison of velocity and area at the test point is used to show the modeling ability of the FPDE and baseline models. Compare with the velocity field in baseline model, FPDE model learns better in large-scale fluctuations.

The difficulty in modeling the arterial flow data lies in the significant difference between the theoretical vessel model, which is used to derive the equations, and real-world vessels. The NN prediction at point 5 is tested (shown in Fig.10.b) in the Y-shaped artery with measurement data. The comparison is shown in Fig.14. As it demonstrated in the theoretical derivation in section 2.1, filter operations do not make NN learn the small-scale fluctuations more finely, but they do make NN model the large-scale information more precisely. On the large-scale of the velocity field, the FPDE model is less likely to become trivial than the baseline model. Even though the measurement doesn't contain any data on pressure, NN still gives a prediction of the pressure field through the physical constraints. Since the FPDE model is more accurate in the velocity field, it is intuitive that it has better prediction in the pressure field. Because the equations only constrain the x-direction derivative of pressure, Fig.14 only shows the NN prediction of pressure individually.

4.2 Existence of ‘conflict’ in loss analysis

In the motivation part (section 2), we theoretically demonstrate the existence of conflict and how the conflict affects the co-optimization process. In our illustration, the conflict can be simply described as the ‘difference between the PDE and data loss optimization direction’. Therefore, we analyze the training losses and find the intuitive data evidence in Fig.15.

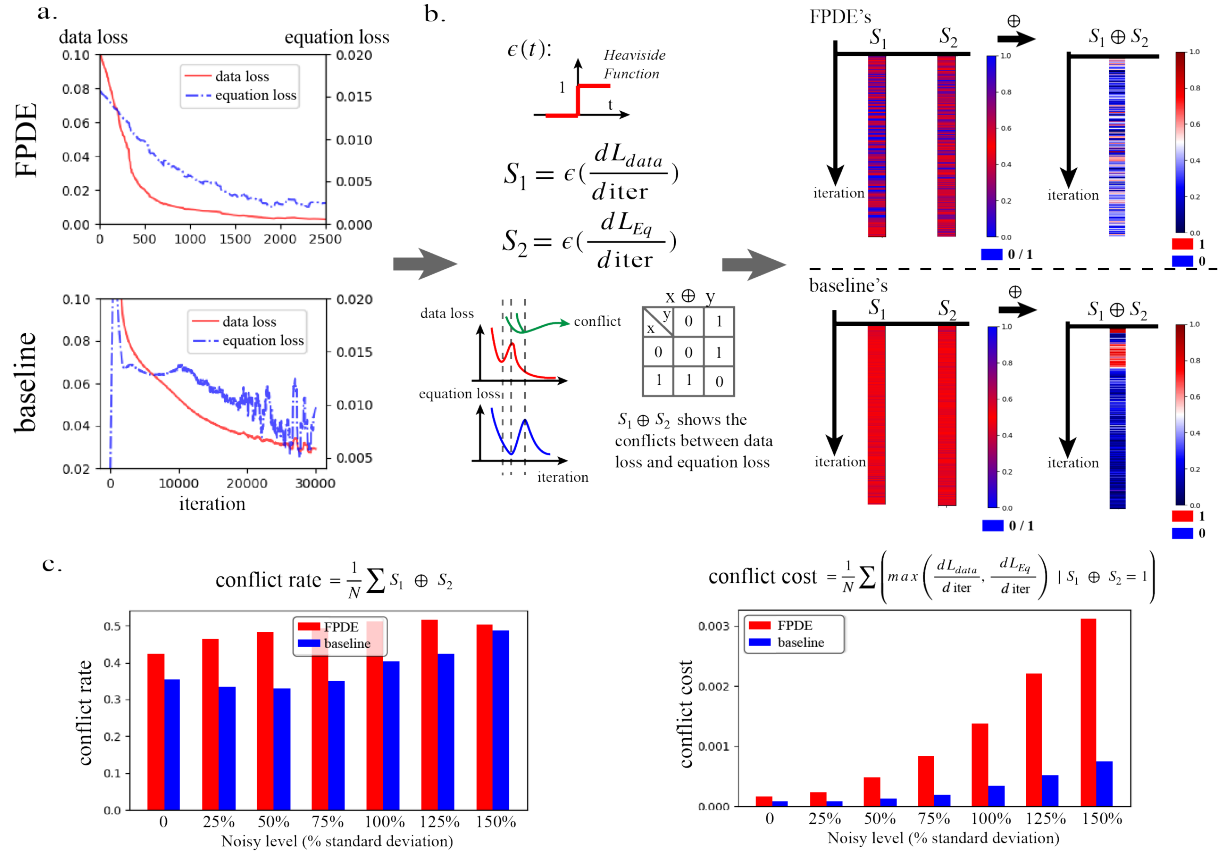


Fig. 15. Decoupling achieved by the FPDE method (reflected in training loss). (a) The PDE and data losses of two models until convergence. (b) The S and ‘exclusive OR’ color bars. In order to show the distribution of the derivative sign, the color bar is used in the after-pooling data of the original S. In the S plot, closer to red means more 0-1 oscillating and no effective gradient descent. In the $S_1 \oplus S_2$ plot, blue color indicates no conflict training process. Therefore, the effective descent in the baseline model only happened in the initial part, while the FPDE model realized decoupling throughout the whole training. (c) The definition and statistic result for each group of the conflict rate and conflict cost, which indicates higher conflict tolerance of FPDE than baseline.

The comparison between the FPDE model (up) and baseline model (down) is shown in Fig.15.a and Fig.15.b. Fig.15.a shows the equation loss and data loss of the FPDE and baseline model in the same experiment. In the baseline model, the equation loss is the original PDE loss. Besides, the equation loss is the filtered PDE loss in the FPDE model. To analyze the correlation of the loss decreasing, we defined S_1 and S_2 as the sign of the equation and data loss derivative. To facilitate the following treatments, the Heaviside function is used to replace the sign operation. Thus, the losses are transferred to the 0/1 lists S, which show the increase or decrease in this iteration. But the 0/1 list is not straightforward, so we change it to blue-red-blue color bar for better demonstration. Specifically, we first average pooling the original data of S and then map the after-pooling data to the blue-red-blue color bar (the color bar on the S left). Therefore, the S bars represent the randomness of loss as they changes by color. Because 0 and 1 represent the direction of loss change, the red color in the middle of the color bar indicates that there is oscillation in this section of the loss. Therefore, when S is in red, the training loss is oscillating, which means the optimization has no effective decrease. Conversely, when the color of the S bar is closed to blue, it means the training loss tends to steadily decrease or increase in this segment.

From the color of S_1 and S_2 bar, it is obvious that the S_1 and S_2 of baseline model in Fig.15.b are almost pure red. Meanwhile, the FPDE model’s still have many blue segments. This indicates that the

baseline model is more unstable, whereas the FPDE model can optimize effectively.

The last two bars in Fig.15.b are the $S_1 \oplus S_2$ bar. S_1 and S_2 are used to show the directions of losses, thus the \oplus (exclusive OR, xor in short) can be used to show the consistency of S_1 and S_2 . If S_1 and S_2 are inconsistent ($S_1 \oplus S_2 = 1$), that means there exist conflict in the co-optimization process. The $S_1 \oplus S_2$ bar is obtained by the exclusive OR solution of the S_1 and S_2 bars, where 1 means the direction between equation and data loss is different and 0 means the same. After pooling operation, the original data is also plotted with a red-white-blue color bar, where red represents conflicts and blue represents no conflicts.

The color of the baseline model in $S_1 \oplus S_2$ shows the conflicts only exist during the initial fast decline segment, and the co-optimization is avoiding the potential conflict and trapping itself in the local optimum in the following segments. Meanwhile, the color in FPDE shows the stochastic conflicts that happened, and the co-optimization does not pay much attention to the potential conflicts, which helps it find the global optimal.

$$\begin{aligned} \text{conflict rate} &= \frac{1}{N} \sum S_1 \oplus S_2 \\ \text{conflict cost} &= \frac{1}{N} \sum \left(\max \left(\frac{dL_{data}}{dL_{train}}, \frac{dL_{pde}}{dL_{train}} \right) \mid S_1 \oplus S_2 = 1 \right) \end{aligned} \quad (17)$$

In Fig.15.c, two statistical indicators are proposed to illustrate Fig.15.b is not a single case. The conflict rate is defined as the frequency of 1 in $S_1 \oplus S_2$ bar, and the conflict cost as the mean derivative of the increasing loss when the conflict happened (shown in Eq.17). These indicators are calculated on a group of losses with increasing noise and plot for the general comparison. Though the two indicators all rise with the level of noise, the baseline model still prioritizes avoiding conflict in order to have a lower conflict rate and cost. The higher conflict in the FPDE reflects the decoupling process, which means the correlation between FPDE loss and data loss is decreased (how the decoupling helps co-optimization and smooth potential local optimums is shown in Fig.7, section 3.2).

In conclusion, the FPDE constraints actually decrease the relevance of PDE and data loss. In the co-optimization process, the FPDE model can still optimize when facing higher conflict. Experiments shows that the FPDE model outperformed the conventional PDE model as a result of the decoupling enhancement in section 3.2. This indicates that the FPDE model can more effectively overcome the noise and sparsity of data from measurements of real-world problems.

5 Conclusion

Since the data in real-world problems is often insufficient and noisy, it is necessary to improve the learning ability and robustness of the model. In other words, reducing NN dependence on data quality and quantity is a necessary prerequisite in the modeling of real-world data. One of the difficulties in the training of a physics-informed model is the conflict in the co-optimization. In this paper, we analyzed the causes of the conflict and propose the FPDE method to overcome it. The improvement of the proposed FPDE is verified in three aspects: theoretical derivation, experiments on the simulation data, and the experiments on real-world measurement data. In the comparison between the FPDE and baseline models, the proposed FPDE constraints have the following characteristics:

- FPDE is a general approach that applies to a variety of models, it is not designed for specific equations or NN architectures. As a surrogate constraint, it has good transferability in most cases.
- The FPDE method can help NN model the noisy and sparse observation data better. This improvement is important for the practical applications of the physics-informed framework.
- The FPDE method can better optimize NN when facing mismatches between the data and equations or the equation coefficients are missing.

Physics-informed methods have proliferated in recent years, and the FPDE surrogate constraint reduces the dependence of the model on data quality and quantity. Although FPDE still cannot handle the

extremely complex problems (e.g., the restoration of 3-dimensional turbulence) like other conventional methods, it performs better in the modeling of real-world problem with sparse and noisy data, which is desired in practice. Furthermore, the use of FPDE is very simple, and it can be applied to other models by replacing the original equation constraints with filtered equations in the training process.

Appendix A Influence of filter’s type in FPDE

In this experiment, the FPDE models with different filters are trained with the same observation data. Thus, the accuracy of results is only determined by the type of filter. The observation data of cylinder flow with a 75% standard deviation of noise is used. For comparison, the conventional physics-informed model is trained as the control group (i.e., No filter in Fig.16). The mean squared errors (MSE) of the results are shown in the figure below (Fig.16).

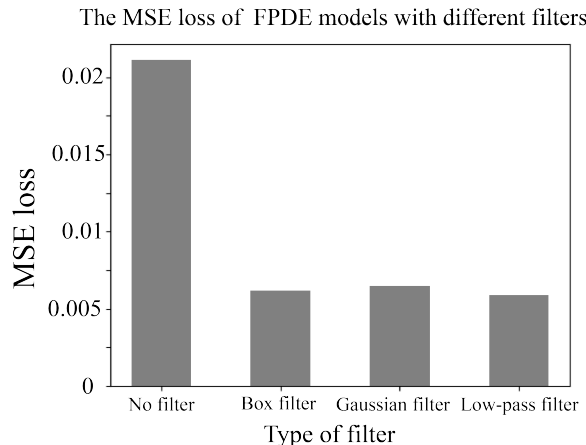


Fig. 16. The MSE of the FPDE models with different filters (including ‘no-filter’). In this experiment, the chosen classic filters are the box filter, the Gaussian filter, and the low-pass filter. The conventional no-filter model is trained as the control group.

The results illustrate that all the given filters in FPDE can improve the training result. Compared to the no-filter group, the improvements of different filters have no significant difference. The result indicates that the FPDE method is robust to different filters and is not sensitive to the selection of filters.

Appendix B Details of cylinder flow

In this experiment, the selected computation case is the 2-dimensional cylinder flow (shown in 1.1, the background information). The cylinder flow, which is governed by the N-S equation, is widely studied due to its complex features. Under the small Reynolds number (Re) condition, the fluid in the cylinder flow case shows the state of Stokes flow or creeping flow[41], which can be simply linearized to the solution of the steady N-S equation. The fluid becomes turbulence as Re increases, and the velocity field shows periodicity. In the vorticity field, the famous Karman vortex street phenomenon appears[42].

The reference IC/BC conditions of the cylinder flow case are from the open resource data in the Supplementary of HFM[32], which is generated by OpenFOAM. In this case, the initial condition and boundary condition are:

$$\begin{aligned}
 u(-10, y) &= (1, 0) \\
 u\left(\frac{1}{2}\cos\theta, \frac{1}{2}\sin\theta\right) &= (0, 0), \quad \theta \in [0, 2\pi]
 \end{aligned}
 \tag{18}$$

where zero pressure outflow and periodicity conditions are imposed in the boundary of $[-10, 30] \cdot [-10, 10]$ simulation domain, and the simulation data is selected in $[-2.5, 7.5] \cdot [-2.5, 2.5]$ area.

This simulation data satisfied the N-S equation, which is the ideal observation data in the condition written in Prop.1. In order to do the restoration in the Fig.2.b, two groups of experiments are designed to

show the FPDE performances with the different data quality and quantity. Assume that data quality and quantity can be summarized as its noise level and sparse level, thus the simulation data of two groups is shown in Table.1. To apply the control variate method, every case in each group has two parallel models. The only difference between two parallel models is the constraint of PDE or FPDE loss. The conventional PDE guided model is used as the baseline model for this question, using the same data in both models during each pair of experiments. In order to balance the additional computational cost caused by filter operation in the FPDE model, the batch size of the baseline model is scaled up k times (k is the filter size). Each model is trained for 50,000 iterations and tested in the whole selected domain ($x \in [-2.5, 7.5]$, $y \in [-2.5, 2.5]$ and $t \in [0, 16]$). Thus, the comparison reflects the improvement of the FPDE constraint compared to the conventional PDE constraint.

In the generation of sparse data in Group 1, the datasets are randomly sampled by the decreasing sampling ratios in Table.1. Seven datasets with different sizes are used as the variables of Group 1 to show the NN restoration ability with the different data missing levels. Obviously, the less observation it has, the more inaccuracy it produces.

In Group 2, noise is added to the $[u, v, p]$ field to make training more difficult (as demonstrated in Prop.2). The ‘additive white Gaussian noise’ (AWGN), the most common noise in the noise analysis, is chosen as the artificial noise added in 2^{-10} sampled dataset. The variances of the noise in $[u, v, p]$ are jointly decided by the standard deviation in $[u, v, p]$ and the noisy rate r ($\epsilon_u = N(0, r \cdot std_u)$). Seven datasets of different noisy levels are used as the variables of Group 2 to show the flow restoration ability with the different data error levels. Obviously, the more noise it has, the more inaccuracy it produces.

The entire simulation data is divided into 3 parts: the training, validation, and test datasets. To test the restoration ability, the restoration outputs are plotted across the entire domain. The division is shown in Fig.17.

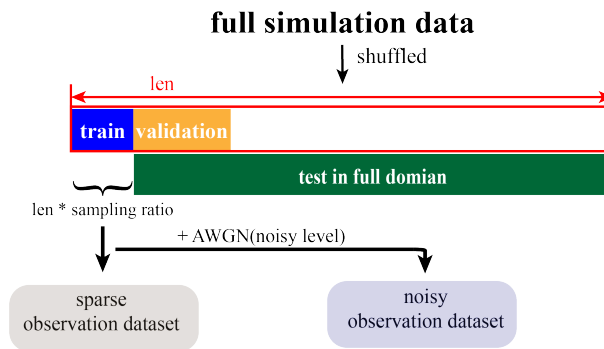


Fig. 17. The pre-processing in full simulation data. In the experiments, the training data is randomly sampled in full dataset. In sparse group, the sampling ratio is the adjustable variable. In noisy group, the noisy level is the adjustable variable.

The training process terminates when the training loss has converged. The final loss function in Eq.4 can be written as follows. When training the FPDE model, the variables $y = (u, v, p)$ are filtered first and calculated in the same form as Eq.12. Each L2 error in the training process is recorded for analysis. The NN parameters are saved every 100 iterations and every iteration with the smallest validation loss.

Appendix C Details of cell migration

In Eq.13, the constants D, λ and K are always obtained by regression. In the experiments, these constants can be obtained by the ordinary least squares (OLS) method with measurement data. Furthermore, the simplified equations are obtained in the knowledge discovery field in Eq.19. [43]

$$\begin{aligned} \frac{\partial C}{\partial t} &= 530.39 \frac{\partial^2 C}{\partial x^2} + 0.066C - 46.42C^2, \quad n = 14,000 \\ \frac{\partial C}{\partial t} &= 982.26 \frac{\partial^2 C}{\partial x^2} + 0.078C - 47.65C^2, \quad n = 20,000 \end{aligned} \quad (19)$$

where n is the initial cell number. In this equation, the coefficients D, λ, K are decided by initial cell number (n), which means the initial density of cell can effect the scratch recover process.

The measurement data is generated by the cell migration experiment in square petri dishes. Cells gradually fill in the scratch by migrating over time, while the densities between the blue lines are counted every 12 hours. Four parallel experiments with different initial cell numbers ($n = 14,000 / 16,000 / 18,000 / 20,000$) are measured to show the effect of n on cell density. The example of real measured data is shown in Fig.9.c, which y-axis represents the cell density between adjacent blue lines ($cells/\mu m^2$) and x-axis is the location (μm). The density data in $t = 0$ is used as the initial data, and the other data ($t = 12h/24h/36h/48h$) is the NN need to predict.

Obviously, the measurement data is high noisy and replication of the experiment is expensive. The data is so sparse in the dimension of n (cell number) that it is impossible to find all coefficients for each n . In terms of the NN training, it is particularly important that the collocation points can't be selected randomly because of the unknown coefficients. Thus it only has the collocation points in $n = 14,000$ and $20,000$ flat to calculate Eq.19. The task is modeling the distribution of unknown equations ($n \in (14,000, 20,000)$) by the conventional PDE/FPDE method. The training data distribution is shown in Fig.18.

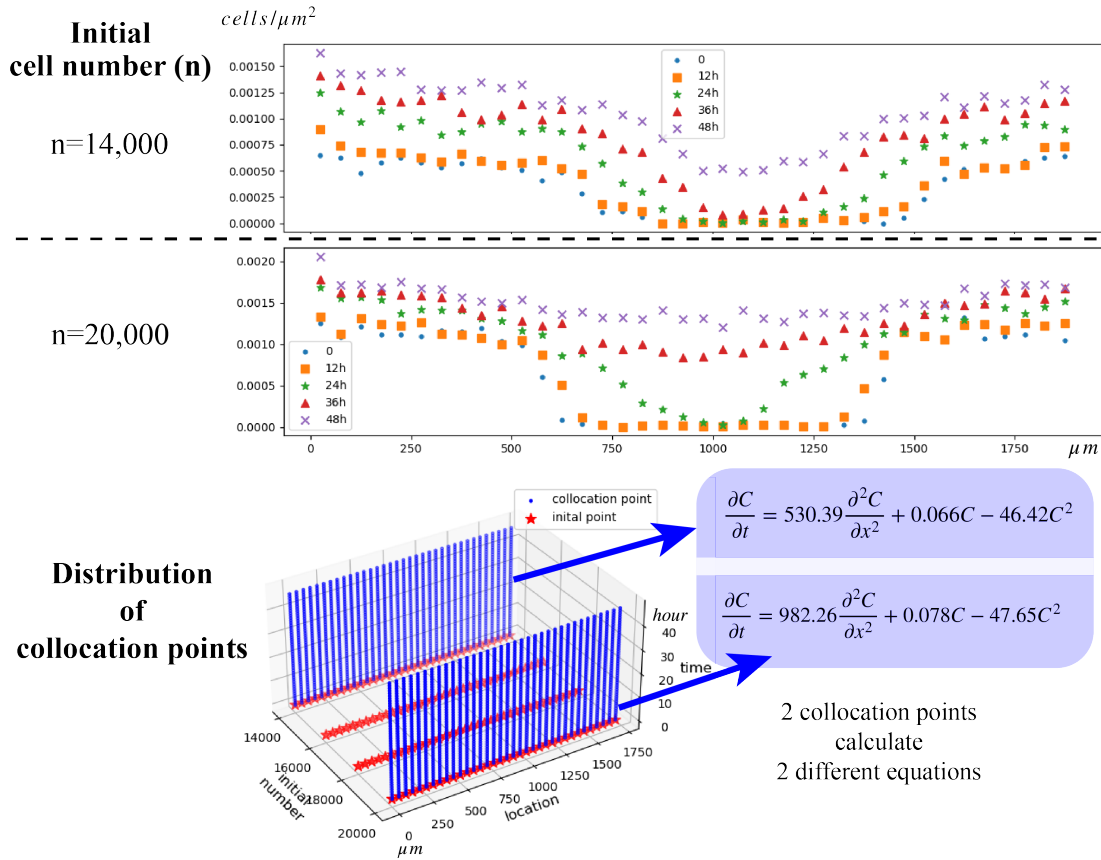


Fig. 18. The training data in cell migration modeling. The dataset's initial cell numbers are 14,000 and 20,000 for the NN training. Depending on the initial cell number, different groups fill the scratch at different speeds.

Data and materials availability

All codes used in this manuscript are publicly available on GitHub at **this repository**. Additional data related to this paper may be requested from the authors.

References

- [1] Mojzesz Kirszbraun. Über die zusammenziehende und lipschitzsche transformationen. *Fundamenta Mathematicae*, 22(1):77–108, 1934.

- [2] Maria Littmann, Katharina Selig, Liel Cohen-Lavi, Yotam Frank, Peter Hönigschmid, Evans Kataka, Anja Mösch, Kun Qian, Avihai Ron, Sebastian Schmid, et al. Validity of machine learning in biology and medicine increased through collaborations across fields of expertise. *Nature Machine Intelligence*, 2(1):18–24, 2020.
- [3] T DebRoy, T Mukherjee, HL Wei, JW Elmer, and JO Milewski. Metallurgy, mechanistic models and machine learning in metal printing. *Nature Reviews Materials*, 6(1):48–68, 2021.
- [4] John W Goodell, Satish Kumar, Weng Marc Lim, and Debidutta Pattnaik. Artificial intelligence and machine learning in finance: Identifying foundations, themes, and research clusters from bibliometric analysis. *Journal of Behavioral and Experimental Finance*, 32:100577, 2021.
- [5] Congyu Wang and Kaiping Peng. Ai experience predicts identification with humankind. *Behavioral Sciences*, 13(2):89, 2023.
- [6] David Vernon. *Machine vision: Automated visual inspection and robot vision*. Prentice-Hall, Inc., 1991.
- [7] Ivan A Sag, Timothy Baldwin, Francis Bond, Ann Copestake, and Dan Flickinger. Multiword expressions: A pain in the neck for nlp. In *International conference on intelligent text processing and computational linguistics*, pages 1–15. Springer, 2002.
- [8] Zongyi Li, Nikola Kovachki, Kamyar Aizzadenesheli, Burigede Liu, Kaushik Bhattacharya, Andrew Stuart, and Anima Anandkumar. Fourier neural operator for parametric partial differential equations. *arXiv preprint arXiv:2010.08895*, 2020.
- [9] Zelong Yuan, Chenyue Xie, and Jianchun Wang. Deconvolutional artificial neural network models for large eddy simulation of turbulence. *Physics of Fluids*, 32(11):115106, 2020.
- [10] Tianyi Li, Michele Buzzicotti, Luca Biferale, Fabio Bonaccorso, Shiyi Chen, and Minping Wan. Data reconstruction of turbulent flows with gappy pod, extended pod and generative adversarial networks. *arXiv preprint arXiv:2210.11921*, 2022.
- [11] Sebastian Ruder. An overview of gradient descent optimization algorithms. *arXiv preprint arXiv:1609.04747*, 2016.
- [12] Kunihiko Fukushima and Sei Miyake. Neocognitron: A self-organizing neural network model for a mechanism of visual pattern recognition. In *Competition and cooperation in neural nets*, pages 267–285. Springer, 1982.
- [13] Han Zhang, Ian Goodfellow, Dimitris Metaxas, and Augustus Odena. Self-attention generative adversarial networks. In *International conference on machine learning*, pages 7354–7363. PMLR, 2019.
- [14] Maziar Raissi, Paris Perdikaris, and George E Karniadakis. Physics-informed neural networks: A deep learning framework for solving forward and inverse problems involving nonlinear partial differential equations. *Journal of Computational physics*, 378:686–707, 2019.
- [15] Lu Lu, Xuhui Meng, Zhiping Mao, and George Em Karniadakis. Deepxde: A deep learning library for solving differential equations. *SIAM Review*, 63(1):208–228, 2021.
- [16] Mengge Du, Yuntian Chen, and Dongxiao Zhang. Autoke: An automatic knowledge embedding framework for scientific machine learning. *arXiv preprint arXiv:2205.05390*, 2022.
- [17] Feiyu Chen, David Sondak, Pavlos Protopapas, Marios Mattheakis, Shuheng Liu, Devansh Agarwal, and Marco Di Giovanni. Neurodiffee: A python package for solving differential equations with neural networks. *Journal of Open Source Software*, 5(46):1931, 2020.
- [18] Yuntian Chen and Dongxiao Zhang. Integration of knowledge and data in machine learning. *arXiv preprint arXiv:2202.10337*, 2022.
- [19] Samuel H Rudy, Steven L Brunton, Joshua L Proctor, and J Nathan Kutz. Data-driven discovery of partial differential equations. *Science advances*, 3(4):e1602614, 2017.
- [20] Hao Xu, Haibin Chang, and Dongxiao Zhang. Dl-pde: Deep-learning based data-driven discovery of partial differential equations from discrete and noisy data. *arXiv preprint arXiv:1908.04463*, 2019.

- [21] Yuntian Chen, Yingtao Luo, Qiang Liu, Hao Xu, and Dongxiao Zhang. Any equation is a forest: Symbolic genetic algorithm for discovering open-form partial differential equations (sga-pde). *arXiv preprint arXiv:2106.11927*, 2021.
- [22] George S Misyris, Andreas Venzke, and Spyros Chatzivasileiadis. Physics-informed neural networks for power systems. In *2020 IEEE Power & Energy Society General Meeting (PESGM)*, pages 1–5. IEEE, 2020.
- [23] Yuntian Chen, Dou Huang, Dongxiao Zhang, Junsheng Zeng, Nanzhe Wang, Haoran Zhang, and Jinyue Yan. Theory-guided hard constraint projection (hcp): A knowledge-based data-driven scientific machine learning method. *Journal of Computational Physics*, 445:110624, 2021.
- [24] Khemraj Shukla, Patricio Clark Di Leoni, James Blackshire, Daniel Sparkman, and George Em Karniadakis. Physics-informed neural network for ultrasound nondestructive quantification of surface breaking cracks. *Journal of Nondestructive Evaluation*, 39(3):1–20, 2020.
- [25] Chulin Wang, Eloisa Bentivegna, Wang Zhou, Levente Klein, and Bruce Elmeegreen. Physics-informed neural network super resolution for advection-diffusion models. *arXiv preprint arXiv:2011.02519*, 2020.
- [26] Nanzhe Wang, Dongxiao Zhang, Haibin Chang, and Heng Li. Deep learning of subsurface flow via theory-guided neural network. *Journal of Hydrology*, 584:124700, 2020.
- [27] Eric J Hartman, James D Keeler, and Jacek M Kowalski. Layered neural networks with gaussian hidden units as universal approximations. *Neural computation*, 2(2):210–215, 1990.
- [28] Roger Temam. *Navier–Stokes equations and nonlinear functional analysis*. SIAM, 1995.
- [29] CY Wang. Exact solutions of the steady-state navier-stokes equations. *Annual Review of Fluid Mechanics*, 23(1):159–177, 1991.
- [30] Roland Glowinski and Olivier Pironneau. Finite element methods for navier-stokes equations. *Annual review of fluid mechanics*, 24(1):167–204, 1992.
- [31] Michael Schäfer, Stefan Turek, Franz Durst, Egon Krause, and Rolf Rannacher. Benchmark computations of laminar flow around a cylinder. In *Flow simulation with high-performance computers II*, pages 547–566. Springer, 1996.
- [32] Maziar Raissi, Alireza Yazdani, and George Em Karniadakis. Hidden fluid mechanics: Learning velocity and pressure fields from flow visualizations. *Science*, 367(6481):1026–1030, 2020.
- [33] Ian J Goodfellow, Oriol Vinyals, and Andrew M Saxe. Qualitatively characterizing neural network optimization problems. *arXiv preprint arXiv:1412.6544*, 2014.
- [34] Joseph Smagorinsky. General circulation experiments with the primitive equations: I. the basic experiment. *Monthly weather review*, 91(3):99–164, 1963.
- [35] Ugo Piomelli. Large-eddy simulation: achievements and challenges. *Progress in aerospace sciences*, 35(4):335–362, 1999.
- [36] GX Cui, CX Xu, and ZS Zhang. Progress in large eddy simulation of turbulent flows. *Acta Aerodynamica Sinica*, 22(2):121–129, 2004.
- [37] John G Saw, Mark CK Yang, and Tse Chin Mo. Chebyshev inequality with estimated mean and variance. *The American Statistician*, 38(2):130–132, 1984.
- [38] Ronald A Howard. *Dynamic programming and markov processes*. 1960.
- [39] Wang Jin, Esha T Shah, Catherine J Penington, Scott W McCue, Lisa K Chopin, and Matthew J Simpson. Reproducibility of scratch assays is affected by the initial degree of confluence: experiments, modelling and model selection. *Journal of theoretical biology*, 390:136–145, 2016.
- [40] Georgios Kissas, Yibo Yang, Eileen Hwuang, Walter R Witschey, John A Detre, and Paris Perdikaris. Machine learning in cardiovascular flows modeling: Predicting arterial blood pressure from non-invasive 4d flow mri data using physics-informed neural networks. *Computer Methods in Applied Mechanics and Engineering*, 358:112623, 2020.

- [41] MD Chilcott and John M Rallison. Creeping flow of dilute polymer solutions past cylinders and spheres. *Journal of Non-Newtonian Fluid Mechanics*, 29:381–432, 1988.
- [42] R Wille. Karman vortex streets. *Advances in Applied Mechanics*, 6:273–287, 1960.
- [43] Zhao Chen, Yang Liu, and Hao Sun. Physics-informed learning of governing equations from scarce data. *Nature communications*, 12(1):1–13, 2021.